J. Fluid Mech. (2024), *vol*. 999, A6, doi:10.1017/jfm.2024.685

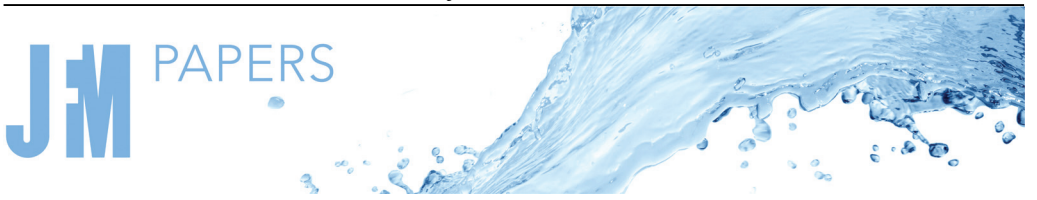

Entrainment of the shear layer separated from a wall-mounted fence

Sicheng Li[1] **and Jinjun Wang**[1],†

[1]Fluid Mechanics Key Laboratory of Education Ministry, Beihang University, Beijing 100191, PR China

(Received 19 November 2023; revised 20 June 2024; accepted 26 June 2024)

Turbulent entrainment at the turbulent/non-turbulent interface (TNTI) plays an important role in understanding the turbulent diffusion. While entrainment in fully developed canonical turbulent flows has been extensively studied, the evolution of entrainment in spatially developing flows remains poorly understood. In this work, characteristics of entrainment and the effect of vortices on entrainment of the shear layer separated from a wall-mounted fence are studied by the experiment in a water channel. The shedding vortex experiences a series of stages, including generation, growth, deformation and breakdown into smaller vortices. With the development of the flow, entrainment varies correspondingly. The prograde vortex near the TNTI is found to suppress entrainment but have little effect on the detrainment process, while the retrograde vortex promotes entrainment and suppresses detrainment as well. Consequently, the local entrainment velocity is decreased by the prograde vortex and increased more significantly by the retrograde vortex. Along the streamwise direction, the time-mean entrainment velocity is smallest where the prograde vortex is strongest in the vortex deformation stage. However, the largest time-mean entrainment velocity is located where the enstrophy gradient near the TNTI is greatest after reattachment, rather than where the retrograde vortex is strongest shortly after the breakdown of the shedding vortex, because the scarcity of retrograde vortices in the vicinity of the TNTI makes their long-time cumulative contribution not as significant as their local enhancement. The present study reveals how entrainment evolves in the separated and reattaching flow, and improves our understanding of the effect of vortices on entrainment.

Key words: boundary layer separation, intermittency, turbulent mixing

1. Introduction

In many turbulent flows, such as jets, mixing layers and turbulent boundary layers, the flow field can be divided into two distinct regions: the turbulent region characterized

† Email address for correspondence: jjwang@buaa.edu.cn

by high-vorticity fluids and the non-turbulent region where the flow is theoretically irrotational (Corrsin & Kistler 1955). These two regions are separated by a thin and strongly convoluted interface known as the turbulent/non-turbulent interface (TNTI), across which turbulent entrainment occurs (da Silva *et al.* 2014*a*). Entrainment refers to the process where irrotational fluids become part of the turbulent region, which is responsible for the transfer of mass, momentum and energy between the turbulent flow and the adjacent non-turbulent flow. In view of its importance in the understanding of turbulent mixing, extensive efforts have been dedicated to identifying, quantifying and modelling entrainment in previous studies (Holzner & Luthi 2011; Wolf *et al.* 2013; Jahanbakhshi & Madnia 2016; Mistry *et al.* 2016; Jahanbakhshi 2021; Long, Wang & Pan 2022*a*; Xu, Long & Wang 2023; Zhang, Watanabe & Nagata 2023).

It is generally agreed that the entrainment process consists of two mechanisms: nibbling and engulfment (da Silva *et al.* 2014*a*). Nibbling refers to the mechanism by which the fluids near the TNTI acquire vorticity due to vorticity diffusion and becomes part of the turbulent region, and engulfment refers to the process in which the irrotational fluids are drawn directly into the turbulent region before they acquire vorticity (Mathew & Basu 2002; Taveira *et al.* 2013; Chauhan, Philip & Marusic 2014; da Silva *et al.* 2014*a*; Jahanbakhshi & Madnia 2016). Nibbling occurs continuously on almost the entire TNTI and is usually considered to be related to the outward spreading of small-scale vortices in the vicinity of the TNTI (Mathew & Basu 2002; Westerweel *et al.* 2005). In recent studies, the nibbling mechanism is generally quantified by the local entrainment velocity, defined as the velocity of the TNTI relative to the flow, which is of Kolmogorov scale and dominated by the viscous component (Holzner & Luthi 2011; Jahanbakhshi & Madnia 2016; Mistry *et al.* 2016; Long *et al.* 2022*a*). Engulfment takes place occasionally and is mostly caused by the motions of large-scale eddies, usually forming low-vorticity pockets (also known as bubbles) in the turbulent region (Mathew & Basu 2002; Taveira *et al.* 2013; Jahanbakhshi & Madnia 2016). As large-scale motions exhibit some distinct characteristics in diverse flows, the contribution of nibbling and engulfment to total entrainment might vary in each flow (Philip & Marusic 2012). For example, it was reported that engulfment is the dominant mechanism in wakes (Bisset, Hunt & Rogers 2002; Hickey, Hussain & Wu 2013), while nibbling plays the main role in the entrainment process in jets and turbulent boundary layers (Mathew & Basu 2002; Westerweel *et al.* 2005; Borrell and Jiménez 2016; Jahanbakhshi & Madnia 2016; Long *et al.* 2022*a*; Xu *et al.* 2023). In view of this fact, it is necessary to discuss the issue of whether nibbling or engulfment contributes more to the entrainment process depending on the specific flow type being considered.

To better understand the mechanisms of entrainment, considerable attention has been devoted to investigating the influence of turbulent coherent structures on entrainment. It was once reported that entrainment is mostly controlled by small-scale motions (Westerweel *et al.* 2005, 2009). The local entrainment velocity is modulated by the nearby Taylor microscale vortex (da Silva *et al.* 2014*a*; Mistry, Philip & Dawson 2019; Neamtu-Halic *et al.* 2020), and statistically, the dominant length scale of TNTI normal velocity is the Taylor microscale (Balamurugan *et al.* 2020). By examining a model where an artificial small-scale eddy is positioned near the TNTI, Watanabe *et al.* (2017) demonstrated that details of entrainment movements are governed by small-scale eddies.

However, since the interaction between scales has been demonstrated to exist at modest Reynolds numbers by recent works (Buxton 2015; Fiscaletti *et al.* 2016*a*,*b*), it seems inappropriate to ignore the contribution of large-scale motions in all cases. In fact, there are many works that emphasized the importance of large-scale motions for turbulent entrainment. Detailed multiscale analyses by Philip *et al.* (2014) and Mistry *et al.* (2016) indicated that although the tortuosity of the TNTI and the local entrainment velocity vary

in different scales, the total entrainment flux is independent of the scale. Philip *et al.* (2014) suggested that viscous effects at the smallest scales provide the physical mechanism ultimately responsible for entrainment, while the overall rate of entrainment is determined by the large-scale transport due to the energy-containing eddies. In addition, Cimarelli & Boga (2021) conducted a numerical study where the large-scale and small-scale velocity fields were numerically separated and evolved independently. They found that entrainment is more intensive in the large-scale velocity field. Long *et al.* (2022*a*) studied the modulations of large-scale motions on entrainment in the turbulent boundary layer. They indicated that high-speed large-scale motions enhance the engulfment by the sweep flow, whereas low-speed large-scale motions induce stronger instantaneous nibbling. Nonetheless, the integral nibbling flux is larger above high-speed motions due to the more distorted TNTI induced by high-speed large-scale motions. Moreover, the Reynolds number dependence of entrainment in the turbulent boundary layer was investigated in a recent study conducted by Zhang *et al.* (2023). The probability density functions (PDFs) of the local entrainment velocity agree well with each other for high Reynolds numbers when the local entrainment velocity is normalized by the friction velocity. They attributed this variation to the diminution of the direct wall effects on the small-scale motions and the prominence of the large-scale motions with the increase of the Reynolds number.

Most previous researches have been limited to the fully developed canonical flows such as jets, wakes, mixing layers and turbulent boundary layers. In contrast, only a few studies have focused on entrainment in more complex flows (Zhang, Rival & Wu 2021; Long, Wang & Wang 2022*b*) or developing flows (Philip *et al.* 2015; Wu, Wallace & Hickey 2019). Zhang *et al.* (2021) studied the TNTI properties in the airfoil flow where separation bubbles, transition, turbulent boundary-layer separation and asymmetric wakes coexist in the complex spatially developing flow. They reported the propensity for local entrainment across the cross-streamwise and leading edges as well as the relatively flat surfaces of the TNTI after the transition, which resembled the behaviour observed in jets (Mistry *et al.* 2019) and wakes (Philip *et al.* 2015). However, in the early transitional stage, entrainment is not strongly influenced by the geometric properties of the TNTI. Long *et al.* (2022*b*) explored the evolution of the TNTI above the main element of a multi-element airfoil. They indicated that the local entrainment flux increases along the streamwise direction, suggesting that the increase in tortuosity of the TNTI has a greater effect on entrainment than the decrease of the vorticity gradient in the transition.

Although many detailed researches have focused on turbulent entrainment, the evolution of entrainment and the effect of flow structures on entrainment in the transition process is not clear yet. In the present work we focuse on turbulent entrainment in the transition of the separated and reattaching flow induced by a fixed fence in the flat-plate boundary layer. Preliminary study has shown that the properties of the TNTI evolve significantly accompanied with the flow evolution from the separated shear layer, transition, reattachment and finally to the turbulent boundary layer (Li, Long & Wang 2022). Whereas, the characteristics of turbulent entrainment in the transition are still unknown and intriguing. In addition, the separated and reattaching turbulent flows, which generally enhance the turbulent mixing, are also ubiquitous and important flows in nature and engineering. From the perspective of the TNTI, the studies on entrainment help to improve our understanding of the turbulent mixing. Therefore, the main objective of the present work is to study the evolution of turbulent entrainment and the effect of vortex structure on entrainment in the separated and reattaching flow.

This paper is organized as follows. The experimental equipment, parameters and the interface detection method are described in § 2. The mean characteristics of the separated and reattaching flow and the dynamics of the shedding vortex are illustrated in § 3.

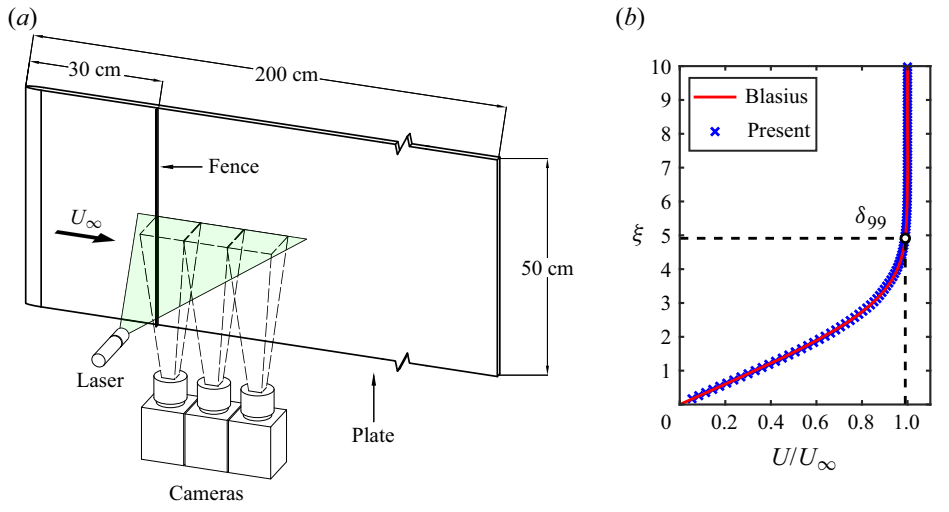

Figure 1. (*a*) Sketch of the experimental set-up. (*b*) Mean profile of the streamwise velocity for the laminar boundary layer.

The streamwise variations of entrainment and the effects of vortex structures on entrainment are studied in § 4. Finally, this paper is summarized in § 5.

2. Experimental methods

2.1. *Experimental set-up*

To analyse the entrainment properties, a time-resolved particle image velocimetry (PIV) experiment was conducted in the low-speed water channel at Beihang University. Actually, the experimental set-up was similar to that in our preliminary study (Li *et al.* 2022) except for the PIV system. Nevertheless, essential parameters are described here again to ensure the integrity of this work and to make it convenient for the reader. As illustrated in figure 1(*a*), a flat and smooth acrylic plate was vertically fixed in the centre of the 3 m long, 60 cm wide channel. The length, width and thickness of the plate were 200, 50 and 1.5 cm, respectively, and the free surface of water just submerged the top of the plate. The ratio of the plate width to the half-width of the flume was 3.33, and the flume was quite wide in the spanwise direction. An elliptic leading edge with the aspect ratio of 5 : 1 was utilized to avoid flow separation from the leading edge of the plate.

To ensure that a stable incoming flow was guaranteed by this experimental set-up, the unperturbed boundary layer on the smooth surface of the plate was examined before installing the fence. Figure 1(*b*) shows the mean profile of the streamwise velocity at the streamwise location where the fence was expected to be installed. The profile compares well with the theoretical velocity profile of laminar boundary layers – the Blasius solution. The vertical coordinate, $\xi = y\sqrt{U_\infty/\nu x_L}$, is the dimensionless similarity variable, where x_L is the streamwise distance from the leading edge of the plate and ν is the kinematic viscosity. The boundary-layer thickness δ_{99} defined by $0.99U_\infty$ is $0.85h$, where $U_\infty = 102$ mm s^{-1} is the free-stream velocity. The shape factor $H = 2.58$, which is quite close to the theoretical value. The Reynolds number based on the displacement thickness δ^* is $Re_{\delta^*} = U_\infty\delta^*/\nu = 286$, which is below the critical value $Re_{\delta^*} \leq 400$ (White 1991). These results suggest that the boundary layer is in a stable laminar state before the fence is installed.

The flow separation was induced by a solid stainless steel fence mounted on the plate, as shown in figure 1(*a*). The fence was 10 mm in height (denoted as h), 1 mm in thickness and 30 cm away from the leading edge of the plate. The fence is as wide as the plate, forming a two-dimensional model with the plate. The Reynolds number based on the height h is $Re_h = U_\infty h/\nu = 965$. The streamwise, vertical and spanwise directions in the laboratory coordinates are denoted as x, y and z, respectively. The x-axis origin was located on the thick centre of the fence, and the y-axis origin was located on the surface of the plate. The streamwise and vertical instantaneous velocities are denoted by u and v, respectively, the corresponding mean velocities are denoted by U and V, respectively, and the fluctuation components are denoted by u' and v', respectively.

The two-dimensional PIV system was used to obtain the velocity field in the side view section (x–y plane). As shown in figure 1(*a*), fields of view (FoV) were located in the central plane of the plate, which were far away from both the free surface and the bottom wall of the channel to reduced the end effect. Seeding particles were hollow glass beads with a diameter of 5–20 μm and a density of 1.05 g cm^{-3}, which were illuminated by a laser sheet approximately 1 mm thick generated by a high-frequency double-pulsed laser (Beamtech Vlite-Hi-527). Particle images were synchronously captured by three CMOS cameras (2048 × 2048 pixels) with Nikkor 85-mm tilt-shift lenses with a sampling frequency of 250 Hz. The FoV for each camera was approximately 100 mm × 100 mm ($10h \times 10h$) and there was an overlap of at least 10 mm between the FoVs of adjacent cameras. Calibration with a single long reference target covering the entire measurement area was used for stitching FoVs. The multiple iterative Lucas–Kanade algorithm (Champagnat *et al.* 2011; Pan *et al.* 2015) was used to calculate the velocity field with an interrogation window of 32 × 32 pixels and an overlap of 75 % for the final iteration. The maximum particle displacement between two adjacent frames was about 9 pixels in all measurements so that the uncertainty for each measurement was kept at the same level. Following Qu *et al.* (2019), the uncertainties of velocity and vorticity are approximately 1.21 mm s^{-1} and 2.32 s^{-1}, respectively. To obtain a velocity field long enough to analyse the evolution of entrainment, three independent measurements were made at different streamwise locations with each measurement covering a streamwise region of approximately 25h, which was limited by the width of the laser sheet.

In the present work, Kolmogorov length scale is defined as $\eta_I = (\nu^3/\varepsilon_I)^{1/4}$, where ε_I is the dissipation rate estimated using the conditional averaging operation (Jahanbakhshi 2021; Zecchetto & da Silva 2021; Zhang *et al.* 2023) based on the assumption of local axisymmetry (George & Hussein 1991),

$$\varepsilon_I = \nu\left[-\overline{\left(\frac{\partial u'}{\partial x}\right)^2}_I + 2\overline{\left(\frac{\partial u'}{\partial y}\right)^2}_I + 2\overline{\left(\frac{\partial v'}{\partial x}\right)^2}_I + 8\overline{\left(\frac{\partial v'}{\partial y}\right)^2}_I\right], \tag{2.1}$$

and the subscript I denotes data measured at the TNTI. As the flow evolves spatially, η_I decreases first and then increases, with its minimum located in the reattachment region where the dissipation rate is the largest. The maximum ratio between the velocity vector spacing δx and η_I is approximately 1.04, indicating that the spatial resolution is high enough. Thus, the present spatial resolution suffices for the TNTI detection and the relevant analysis. In addition, since the Kolmogorov scale is not constant along the whole FoV, all results normalized by the Kolmogorov scale hereinafter are normalized using the local Kolmogorov scale.

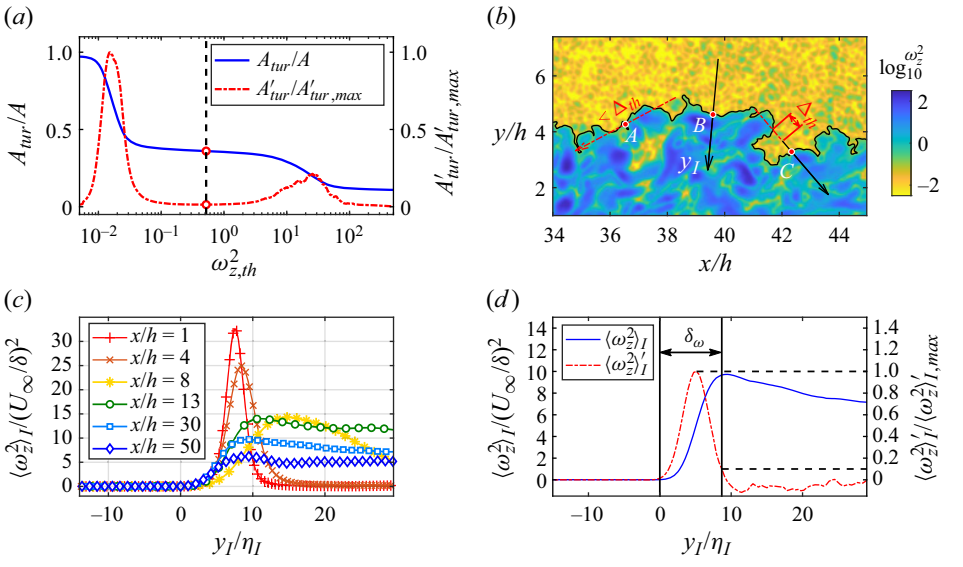

Figure 2. (*a*) Proportion of turbulent area as a function of threshold $\omega^2_{z,th}$. Here A'_{tur} is normalized by the maximum slope $A'_{tur,max}$. (*b*) Local TNTI coordinate y_I. The black curve denotes the instantaneous TNTI. The red dash-dotted lines represent the excluded samples. (*c*) Conditional averaged enstrophy $\langle\omega_z^2\rangle_I$. (*d*) Definition of the mean TNTI thickness at $x = 30h$. $\langle\omega_z^2\rangle'_I$ is normalized by the largest gradient $\langle\omega_z^2\rangle'_{I,max}$.

2.2. *Turbulent/non-turbulent interface detection method*

To study the entrainment properties, the instantaneous interface between the rotational flows and the free stream needs to be detected. Considering the rotational property shared by the separated shear layer, transitional boundary layer and turbulent boundary layer compared with the free stream, the interface is detected by the magnitude of spanwise enstrophy $\omega_z^2 = (\partial v/\partial x - \partial u/\partial y)^2$ with an artificially selected threshold $\omega^2_{z,th}$. Strictly speaking, as the separated shear layer is not initially turbulent (see § 3), it might be debatable to call the interface a TNTI. Nevertheless, the detection procedure is consistent with the detection of TNTI in fully developed turbulence (Zecchetto & da Silva 2021; Long *et al.* 2022*a*). As a consequence, when the downstream boundary layer is fully developed, the present results will be consistent with the existing turbulent entrainment conclusions. For convenience, the interface herein is also referred to as TNTI without a strict distinction following the practice of Philip *et al.* (2015) and Long *et al.* (2022*b*).

By specifying a threshold, the flow field is divided into two regions: the turbulent region where $\omega_z^2 > \omega^2_{z,th}$ and the non-turbulent region where $\omega_z^2 < \omega^2_{z,th}$. To choose the most reasonable threshold, A_{tur}/A against the threshold is examined, where A_{tur} is the mean area of the turbulent region and A is the area of the whole field. Then, the threshold is selected where the slope of this curve $A'_{tur} = |\mathrm{d}A_{tur}/\mathrm{d}\omega^2_{z,th}|$ is minimal, as marked by the hollow circles in figure 2(*a*). From an opposite perspective, the process of detecting the turbulent region is equivalent to the process of detecting the non-turbulent region. Although the flow in the turbulent region evolves gradually downstream of the fence, the enstrophy in the non-turbulent region is generally constant. Therefore, the same threshold is used in the whole FoV for each measurement.

The TNTI is located where the vorticity magnitude is rapidly adjusted between the turbulent and non-turbulent regions (da Silva *et al.* 2014*a*). Therefore, the TNTI is

characterized by a large gradient of the enstrophy across the TNTI, which is usually presented by the conditional averaged enstrophy profile and is widely used to verify the reasonability of TNTI detection (Jahanbakhshi & Madnia 2016; Zhang, Watanabe & Nagata 2018; Long *et al.* 2022*a*). The conditional averaged enstrophy is obtained along the local TNTI coordinate y_I that originates from the instantaneous TNTI and points to the turbulent region along the local unit normal vector $\boldsymbol{n} = \nabla\omega_z^2/|\nabla\omega_z^2|$, as shown in figure 2(*b*). The conditional averaged enstrophy, denoted by $\langle\omega_z^2\rangle_I$, is then calculated by averaging the data collected along the local TNTI coordinate in every instant. Exactly because the geometry of the TNTI is distorted, the local TNTI coordinate will cross the TNTI multiple times at certain positions. A problem arises at these positions where data collected in turbulent and non-turbulent regions are mixed and averaged together. To avoid this problem, data at specified positions are excluded from the conditional averaging (Watanabe, Zhang & Nagata 2018). If the second cross-point is at $|y_I| \leq \Delta_{th}$, all data on this coordinate are excluded, as shown at point A in figure 2(*b*). If the second cross-point is at $|y_I| > \Delta_{th}$, data whose distance from the second cross-point is less than Δ_{th} are excluded, as shown at point C in figure 2(*b*). Here Δ_{th} is set to be $9\eta_I$, and changing Δ_{th} slightly does not affect conclusions.

Figure 2(*c*) shows profiles of the conditional averaged enstrophy at different streamwise positions. The step changes of conditional averaged enstrophy across the detected TNTI at all streamwise positions are clearly presented. In the non-turbulent region outside the TNTI ($y_I < 0$), the enstrophy is almost zero, whereas the enstrophy increases rapidly inside the TNTI ($y_I > 0$). These results suggest that the selected threshold works well for distinguishing the inner turbulent region from the outer non-turbulent region at different streamwise positions.

Furthermore, the mean thickness of the TNTI can be estimated based on the conditional average analysis. Following previous studies (Hayashi, Watanabe & Nagata 2021; Li *et al.* 2022), the mean TNTI thickness δ_ω is defined as the distance from $y_I = 0$ to the position of $\langle\omega_z^2\rangle_I'/\langle\omega_z^2\rangle_{I,max}' = 0.1$, where $\langle\omega_z^2\rangle_I' = \mathrm{d}\langle\omega_z^2\rangle_I/\mathrm{d}y_I$ is the gradient of the conditional averaged enstrophy and $\langle\omega_z^2\rangle_{I,max}'$ is the largest gradient. Profiles of the conditional averaged enstrophy and its gradient at $x = 30h$ are taken, for example, as shown in figure 2(*d*). In the present case, the TNTI thickness at different streamwise positions is less than the value of $15\eta_I$ reported in many fully developed turbulent flows (Zecchetto & da Silva 2021; Long *et al.* 2022*a*; Zhang *et al.* 2023). This might be owing to the effect of a low Reynolds number (Silva, Zecchetto & da Silva 2018; Wu *et al.* 2019; Li *et al.* 2022). Due to the highly similar flow conditions, the streamwise evolution of the TNTI thickness (not shown here) is almost the same with that in our previous work, and more detailed results about the streamwise variation of the conditional averaged quantities can be found in Li *et al.* (2022).

3. Characteristics of the separated and reattaching flow

3.1. *Mean flow characteristics*

Numerous evidence indicates that flow structures have significant effects on turbulent entrainment as mentioned in § 1. Therefore, it is necessary to study the basic characteristics of flow structures before detailed analyses on entrainment. On average, the flow field can be divided into four zones (Agelinchaab & Tachie 2008): (i) the separated shear layer, (ii) separation bubble or recirculation zone beneath the shear layer, (iii) reattachment zone and (iv) recovery region downstream of the reattachment where a new boundary layer develops.

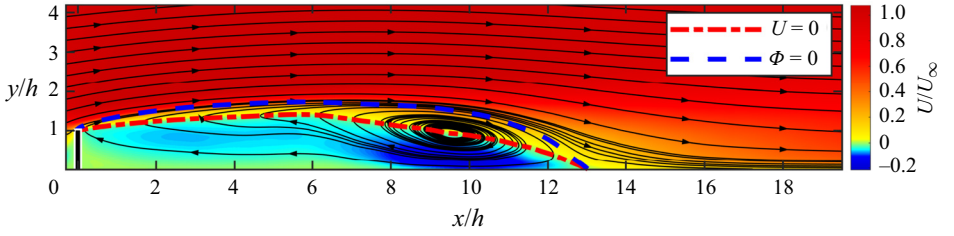

Figure 3. Contour of mean streamwise velocity (U) and mean streamlines.

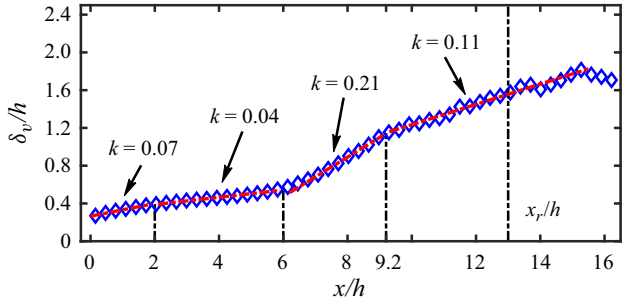

Figure 4. Streamwise variation of vorticity thickness (δ_v). The red dash-dotted lines represent the linear fits to vorticity thickness. Here $k = \mathrm{d}\delta_v/\mathrm{d}x$ is the growth rate of vorticity thickness.

The contour of mean streamwise velocity U superimposed with mean streamlines are shown in figure 3. A large separation bubble can be observed behind the fence. Isopleths of $U = 0$ and $\Phi = 0$ are also superimposed in figure 3, where Φ is the integral of mean streamwise velocity along the vertical direction, i.e. $\Phi(x, y) = \int_0^y U(x, y)\,\mathrm{d}y$. The isopleth of $\Phi = 0$ is considered to be a favourable approximation of the separating streamline (Castro & Haque 1987; Mohammed-Taifour & Weiss 2016; Fang & Tachie 2019), which is the streamline originated from the leading edge of the fence to the reattachment point on the wall. Therefore, isopleths of $U = 0$ and $\Phi = 0$ represent the centre and upper boundary of the mean separation bubble, respectively. The height and length of the separation bubble is $1.7h$ and $13h$ (i.e. the reattachment point is located at $x_r = 13h$), obtained by checking the peak and the intersection point with the wall on the isopleth of $\Phi = 0$, respectively. The size of the separation bubble is quite large and coincides well with the observation reported by van der Kindere & Ganapathisubramani (2018) in the case with the same streamwise aspect ratio of the wall-mounted obstacle.

To further illustrate the growth of the mean separated shear layer, the streamwise variation of the vorticity thickness is employed as shown in figure 4. The vorticity thickness is defined as $\delta_v = (U_{max} - U_{min})/(\partial U/\partial y)_{max}$, where U_{max} and U_{min} are the maximum and minimum mean streamwise velocity, respectively, and $(\partial U/\partial y)_{max}$ is the maximum vertical gradient of the mean streamwise velocity. The vorticity thickness was originally proposed by Brown & Roshko (1974) and is useful for quantifying the growth of the separated shear layer. It is well known that δ_v increase approximately linearly along the streamwise direction with a similar growth rate $k = \mathrm{d}\delta_v/\mathrm{d}x$ in different types of shear layers (Brown & Roshko 1974; Agelinchaab & Tachie 2008; Mohammed-Taifour & Weiss 2016). Moreover, recent studies have shown that k will change with the transition of the shear layer and the development of flow structures (Fang & Tachie 2019; Cheng & Chen 2021; Kang *et al.* 2021; Li *et al.* 2022).

As shown in figure 4, there are four growth rates of the vorticity thickness in the separated region. The growth rate in the range $x = 0$–$6h$ is much smaller than values of $k \in [0.15$–$0.22]$ reported for plane mixing layers and separations over bluff bodies, forward-facing steps and backward-facing steps (Brown & Roshko 1974; Lander *et al.* 2016; Nematollahi & Tachie 2018; Fang & Tachie 2019). The lower growth rate might be due to the absence of initial vortex structures or the absence of major deformation in vortex structures (Martha, Blaisdell & Lyrintzis 2013; Cheng & Chen 2021), which implies the disturbance is weak in this stage. The growth rate becomes $k = 0.21$ in the range $x = 6$–$9.2h$, which is in good agreement with previous results of $k \in [0.15$–$0.22]$. Subsequently, the growth rate decreases to $k = 0.11$ for $x > 9.2h$, which is mainly caused by the decrease of the velocity difference across the shear layer (Agelinchaab & Tachie 2008; Kang *et al.* 2021). Considering that multiple growth rates might suggest different stages of development, the development of the separated shear layer is further divided into four stages by these characteristic points where the vorticity thickness growth rate changes, and characteristics of flow structures corresponding to each stage will be further discussed in § 3.2.

3.2. *Development of the shedding vortex*

Generally, the transition process begins where the instability causes the separated shear layer to roll up and form concentrated centres of vorticity, which leads to the generation of vortices. At a low Reynolds number, the growth and advection of vortices are relatively regular in the early stage of separation. Subsequently, these coherent vortices undergo large three-dimensional deformations due to secondary instability and eventually break down into small turbulent eddies (Lander *et al.* 2016; Moore, Letchford & Amitay 2019). To make the evolution process of the shedding vortex more clear, power spectra of the vertical velocity at different streamwise positions are explored to study the periodicity of the separated flow as shown in figure 5(*a*). The temporal signals for the spectra analysis are extracted at local peaks of the root mean square (r.m.s.) of vertical velocity v_{rms} at different streamwise positions illustrated by the black solid line in the top of figure 5(*a*). The power spectral density (PSD) is estimated by the Welch method (Welch 1967) and normalized by the local variance of vertical velocity. Strouhal number is defined as $St = fh/U_\infty$ here. There are two distinct broad spectral peak bands, i.e. $St_0 \approx 0.19$ (1.9 Hz) and $St_1 \approx 0.14$ (1.4 Hz), as marked by horizontal dashed lines in the bottom of figure 5(*a*). Here St_0 is the first observable characteristic frequency along the streamwise direction that is in good agreement with the vortex shedding frequency reported by Gu, Yang & Liu (2017) ($St \approx 0.18$ at $x/h = 4$) and Fraga, Yin & Ong (2022) ($St \approx 0.2$ at $x/h = 3.5$) where the boundary-layer thickness δ/h is also small. Another characteristic frequency St_1 appearing at $x \approx 6h$ might also be related to the vortex shedding, which is indicated by the wavelet analysis. Wavelets are helpful to study periodic characteristics of time series associated with time-varying frequencies. The wavelet spectrum is computed based on the Morlet wavelet (Morlet 1983). The vertical velocity signal used for the wavelet analysis is extracted in the range where two characteristic frequencies coexist, for example, at $x = 7.5h$, and contains at least 43 vortex shedding cycles. Higher wavelet coefficients are alternately clustered around St_0 and St_1 in the time series as shown in figure 5(*b*), indicating the coexistence of vortex shedding at different frequencies. Since St_1 does not appear and cease synchronously with St_0, the appearance of St_1 indicates a new development stage of the shedding vortex when $x > 6h$.

In addition to the frequency alternation between St_0 and St_1, the frequency migration towards lower frequencies is discernible in the field. This phenomenon is usually related to

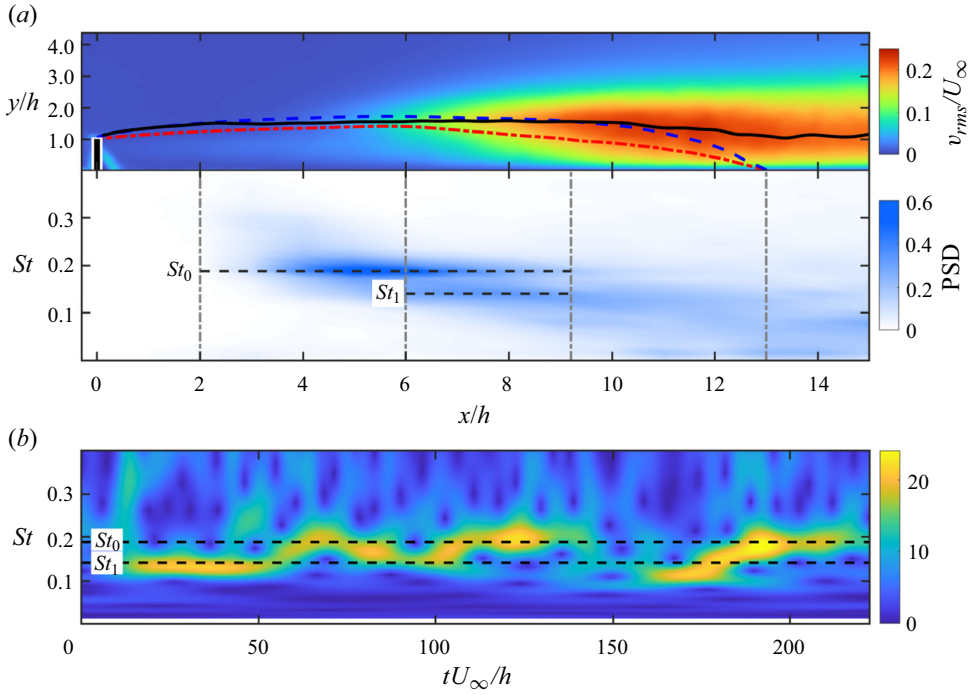

Figure 5. (*a*) The r.m.s. of the vertical velocity (top) and the normalized PSD (bottom) at different streamwise positions. The black solid line (top) represents the locations of the local peaks of v_{rms} at each streamwise position. The superimposed dash-dotted and dashed curves (top) are the same as those in figure 3. The grey vertical dash-dotted lines (bottom) are used as the position references obtained from figure 4. (*b*) Wavelet spectrum of the vertical velocity at $x = 7.5h$.

the behaviour of vortex pairing occurring repeatedly and the complex interaction between vortices at difficult frequencies (Moore *et al.* 2019; Fang, Tachie & Dow 2022). The migration from high to low frequency is continuous rather than discrete, which is similar to the observation by Moore *et al.* (2019) in the latter part of the separation bubble. Fang *et al.* (2022) suggested that the continuous frequency migration is caused by the interruption of the development of Kelvin–Helmholtz (KH) instability by the vortex shedding instability. Actually, there is no discernible spectral peak at much higher frequencies that might correspond to the KH instability, e.g. $St \approx 4$–8 reported by Moore *et al.* (2019) or $St = 3.6$ reported by Fang *et al.* (2022) near the leading edge of bluff bodies. The absence of a KH frequency might be related to the low Reynolds number (Rajagopalan & Antonia 2005) and accordingly suggests that the vortex shedding is the primary instability mechanism in the separated shear layer.

Furthermore, the streamwise evolution of the spectrum shows some rough similarities with that of the vorticity thickness growth rate, as indicated by the vertical dash-dotted lines in figure 5(*a*). Specifically, the normalized PSD is very small when $x < 2h$ compared with the downstream PSD because the disturbance is weak and the separated shear layer is still stable in the early stage. Here St_0 appears at $x = 2h$ where the growth rate of δ_v varies for the first time, and St_1 appears at $x = 6h$ corresponding to the second change of δ_v growth rate. Additionally, the first significant frequency migration begins at approximately $x = 6h$ and the frequency migration towards lower frequencies becomes more frequent and broad when $x > 9.2h$. Generally, the shedding vortex will undergo several development

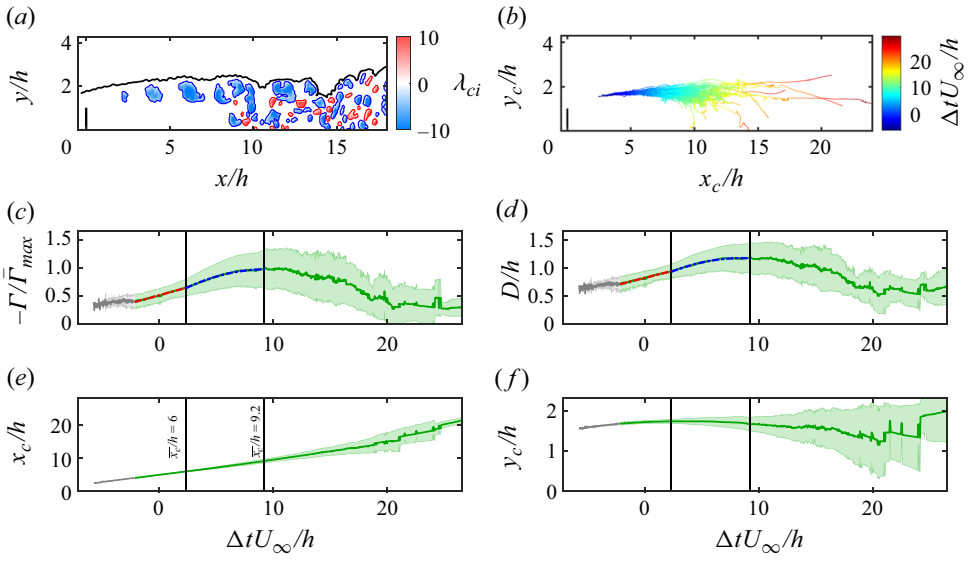

Figure 6. (*a*) Visualization of instantaneous vortex structures detected by λ_{ci} criterion. The TNTI is denoted by the black curve. (*b*) Trajectories of vortex centroids coloured according to the dimensionless time interval $\Delta tU_\infty/h$. Temporal evolution of the (*c*) vortex circulation Γ, (*d*) vortex diameter D, (*e*) vortex centroid x-coordinate x_c and (*f*) vortex centroid y-coordinate y_c. In (*c*,*d*,*e*,*f*) the solid curve and the shaded region represent the mean value and the standard deviation of the corresponding property, respectively. Vertical black solid lines mark the locations where $x_c = 6h$ and $x_c = 9.2h$, respectively. In (*c*,*d*) the red dash-dotted line represents the linear fit to the mean value, and the blue dash-dotted curve represents the second-order polynomial fit to the mean value.

stages, such as growth, deformation due to nonlinear interaction and breakdown (Lander *et al.* 2016). Therefore, it is natural to associate the variations of vorticity thickness growth rate and spectral characteristics along the streamwise direction with the changes in major characteristics of the shedding vortex. However, it seems insufficient to identify the evolution of the shedding vortex based only on the spectra. On the one hand, the spectra do not intuitively show the vortex structures. On the other hand, even if vortex structures break down, the PSD of the predominant frequencies in the spectra will not disappear immediately (Moore *et al.* 2019), which makes it difficult to confirm whether the shedding vortex breaks down after $x > 9.2h$ (statistically speaking). Consequently, to make the evolution of vortices more explicit and quantitative, we conducted the analysis on the instantaneous motion of vortex structures.

Herein, vortex structures are detected using the swirling strength (λ_{ci}) criterion proposed by Zhou *et al.* (1999). In this criterion, the swirling strength of the fluid element is quantified by λ_{ci}, which is the magnitude of the imaginary part of the eigenvalue of the velocity gradient tensor. Nevertheless, because the complete three-dimensional velocity gradient tensor is inaccessible here, the two-dimensional velocity gradient tensor is used in estimating the values of the swirling strength. Vortex detection via swirling strength is Galilean invariant but does not retain the information of the swirling direction. Therefore, the sign of λ_{ci} is set to be the same as that of the local spanwise vorticity to distinguish spanwise vortices with different swirling directions as shown in figure 6(*a*). Clockwise rotating spanwise vortices ($\lambda_{ci} < 0$) are also referred to as prograde spanwise vortices, because they rotate in the same sense as the mean shear. Similarly, counterclockwise rotating spanwise vortices ($\lambda_{ci} > 0$) are also referred to as retrograde spanwise vortices.

Besides, 1.5 times the r.m.s. of λ_{ci} is used as a threshold to limit the influence of noise and detect the boundary of vortex structures (Wu & Christensen 2006; Cui *et al.* 2019).

Based on the time-resolved data, the trajectory of each vortex can be traced to investigate the development of the shedding vortex in a pseudo-Lagrange perspective. Along these trajectories, properties of vortex structures such as circulations Γ, diameters D, x-coordinates x_c and y-coordinates y_c of centroids are recorded in time order. Here, the vortex circulation is estimated as $\Gamma = \int_{\Omega} \omega_z \, \mathrm{d}\sigma$, where $\mathrm{d}\sigma$ is the area element and Ω is the domain of the vortex structure. The vortex diameter is estimated as $D = 2\sqrt{A_v/\pi}$, where A_v is the area of the vortex structure. As shown in figure 6(b), instantaneous trajectories of vortices are disordered because the deformation and breakdown of different vortex structures occur randomly at different locations due to instability. To compare the variation of vorticity thickness and spectra with the evolution of the shedding vortex quantitatively, the conditional mean and standard deviation of vortex structures are calculated based on the time interval Δt from a specific instant t_0, where t_0 corresponds to the instant when the vortex convection passes a certain location $x_c = x_0$. The conclusion does not change when $x_0 = 4$–$6h$ because the motion of a vortex structure is relatively periodical in this region, which is characterized by the significant frequency as shown in figure 5(a). Therefore, statistical results when $x_0 = 5h$ are taken, for example, as shown in figure 6(c–f). Unfortunately, due to the imperfection of the λ_{ci} criterion (Liu *et al.* 2019), when the fluid element in the separated layer is dominant by shear motion, the vortex boundary detection is not very accurate. This disadvantage leads to severe fluctuations of Γ and D when $\Delta t U_\infty/h < -2.2$ ($x_c < 4h$) as shown in figure 6(c,d) coloured in grey. Nevertheless, the λ_{ci} criterion works best for present two-dimensional data sets compared with other vortex identification methods.

Despite this disadvantage, it is clear that both mean circulation $\bar{\Gamma}$ and mean diameter $\bar{D}$ increase almost linearly when $x_c < 6h$, and vary nonlinearly when $x_c > 6h$, which is related to the vortex deformation and nonlinear interaction due to the secondary instability. The standard deviation of y_c increase when $x > 6h$ while the standard deviation of x_c is negligible, which indicates that the vortex deformation leads to vertical fluctuations of the vortex centroid rather than affecting the advection velocity of the vortex. In the vortex tracking process, only one vortex trajectory after the breakdown of the shedding vortex can be connected with the trajectory before. Thus, the circulation and size of the vortex along the trajectory will collapse if the vortex breaks down. As a consequence, the peak of $\bar{\Gamma}$ is expected to be associated with the occurrence of the vortex breakdown. Additionally, when $x_c > 9.2h$, all standard deviations of Γ, D, x_c and y_c further increase obviously, and the mean values of these quantities become more fluctuant due to the significant difference between the trajectories of different small vortices after the breakdown. These characteristic points, $x = 6h$ and $9.2h$, are consistent with that of vortex thickness as shown in figure 4, which further supports the view that statistically speaking, the shedding vortex begins to deform at $x = 6h$ and breaks down at $x = 9.2h$ in the present case.

According to above analyses on the spectra and the vortex tracking, it becomes more reasonable to divide the development of the separated flow into four stages by the characteristic points of the vorticity thickness, i.e. the stage in $x = 0$–$2h$ where the separated layer is laminar, the stage in $x = 2$–$6h$ where the disturbance is small and discrete spanwise vortices appear and grow regularly, the stage in $x = 6$–$9.2h$ where vortices deform significantly due to the secondary instability, and the stage for $x > 9.2h$ where large shedding vortices breaks down into small ones. This division is similar to that in our previous study (Li *et al.* 2022), and is reinforced in different ways here because understanding the vortex evolution is advantageous and necessary to study the relationship between the mechanisms of entrainment and vortex structures.

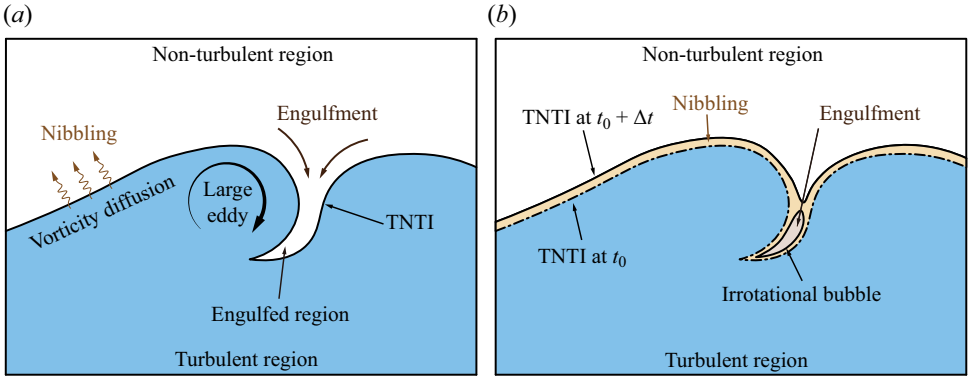

Figure 7. (*a*) Schematic of the entrainment process that consists of the nibbling process and the engulfment processes. (*b*) Schematic of the movement of the TNTI as a result of nibbling and engulfment. For brevity, advection is not presented in this figure.

4. Development of entrainment

To investigate the effect of vortex structures on entrainment during the transition, it is also important to study the variation of entrainment along the streamwise direction. To avoid confusion, it should be noted that the definitions of both nibbling and engulfment may be different in various works. In some multiscale studies (e.g. Philip *et al.* 2014; Mistry *et al.* 2016), engulfment and nibbling are defined as the entrainment process related to large-scale and small-scale components, respectively. In the present work, the traditional anthropomorphic definition is adopted as illustrated in figure 7(*a*), which is the definition generally adopted in most studies (Mathew & Basu 2002; Westerweel *et al.* 2005; Taveira *et al.* 2013; da Silva *et al.* 2014*a*; Jahanbakhshi & Madnia 2016; Long *et al.* 2022*a*,*b*). Engulfment refers to the (inviscid) process in which large-scale eddy motions pull the external fluid into the turbulent region by induced velocity, forming low-vorticity bubbles inside the turbulent region, which happens occasionally. By contrast, nibbling is considered as the continuous movement of the TNTI caused by vorticity diffusion along the whole TNTI. It is proved that nibbling is dominant by viscous diffusion and viscous dissipation (Holzner & Luthi 2011), which are also present in the laminar flow (Philip *et al.* 2015). Therefore, this definition inherently covers the cases where the separation of scales is insufficient in the transition process.

Figure 7(*b*) depicts a concise schematic of the movement of the TNTI from its position at the initial instant t_0 (dash-dotted line) to the position at the subsequent instant $t_0 + \Delta t$ (solid line) as a result of entrainment. The region encompassed between the two instantaneous TNTIs represents the fluid volume entrained into the turbulent region. This entrained volume is composed of two parts, one caused by nibbling that is distributed along the entire TNTI (coloured in pale yellow), and the other stemming from engulfment that is isolated (coloured in light grey). Therefore, one way to evaluate the contribution of nibbling and engulfment to entrainment is to compare the mass (equivalent to volume for incompressible flows) entrained into the turbulent region by each of these mechanisms (Jahanbakhshi & Madnia 2016; Long *et al.* 2022*a*). The contribution of nibbling is usually quantified by the nibbling flux, i.e. the fluid volume across the TNTI per unit area (length for two-dimensional data) in unit time, which is obtained by integrating the entrainment velocity along the TNTI (Jahanbakhshi & Madnia 2016; Mistry *et al.* 2016; Long *et al.* 2022*a*). On the other hand, the contribution of engulfment can be assessed by examining the volume of bubbles. In previous works, for comparing with the nibbling flux,

the contribution of engulfment was measured by an constructed 'flux' that was the total volume of bubbles divided by a characteristic time (Jahanbakhshi & Madnia 2016; Long *et al.* 2022*a*). Whereas, as engulfment is not a continuous mechanism like nibbling, this 'flux' is more of a statistic than a physical quantity. It seems disputable to compare it directly with the nibbling flux that is a physical quantity, and the choice of characteristic time might also affect the results. Consequently, this study shifted to comparing the time-mean volume (actually area for two-dimensional data) entrained by each of these mechanisms over a longer period of time, rather than examining fluxes. More details are presented in §§ 4.1 and 4.2, respectively.

4.1. *Entrainment characteristics: nibbling*

To quantify the nibbling process, the basic idea is to decompose the movement of TNTI into two components: the advection with local flow and the displacement resulting from local nibbling. By subtracting the local advection from the total movement, the component attributable to nibbling is acquired. Subsequently, the instantaneous entrainment velocity v_n is defined as the nibbling-caused displacement per unit time. When nibbling causes the expansion of the turbulent region (i.e. the TNTI moves towards the non-turbulent region), v_n is negative as the TNTI normal vectors are oriented from the non-turbulent region to the turbulent region herein. Conversely, v_n can also be positive denoting the process inverse to entrainment, called detrainment, when the turbulent region experiences a local contraction (Jahanbakhshi & Madnia 2016; Mistry *et al.* 2019; Kankanwadi & Buxton 2020). Specifically speaking, fluids that initially containing vorticity above the threshold defining the TNTI may lose vorticity due to viscous dissipation (Mistry *et al.* 2019), leading to a reduction in their vorticity to levels below the TNTI threshold. Consequently, these fluids leave from the turbulent region into the non-turbulent region, which results in detrainment. Certainly, the mean entrainment velocity remains negative (see figure 9*a*) corresponding to the net expansion of the turbulent region, which is a result of imbalance between local entrainment and local detrainment.

Due to the lack of three-dimensional data, it is difficult to calculate v_n directly through the theoretical formula deduced by Holzner & Luthi (2011). Therefore, v_n is obtained utilizing a TNTI-tracking method proposed by Wolf *et al.* (2012). This method has been used in many previous studies based on two-dimensional data sets, and v_n obtained, which is only a projection of the entrainment velocity on the two-dimensional plane, is sufficient to reflect dominant nibbling characteristics (Mistry *et al.* 2016; Kankanwadi & Buxton 2020; Long *et al.* 2022*a*).

Figure 8(*a*) illustrates the calculation process. First, the TNTI at a short-time interval after $(t_0 + \Delta t)$ is advected with the local velocity back to the current instant t_0, which is called the advected TNTI. Second, the entrainment velocity v_n is obtained by dividing the normal distance from the current TNTI to the advected TNTI with the advection time Δt. In the practice of this method, large errors might be caused by noise when Δt is too small, which could usually be reduced by increasing Δt. However, if Δt is too large, other errors due to the out-of-plane motion and too large spatial evolution of the fluid will become unfavourable to the measurement. The selection of Δt lacks a uniform standard, which depends on the data set and flow type being considered, and whether it is appropriate to select the same Δt in a spatially evolving flow remains to be explored. Mistry *et al.* (2016) studied the effect of Δt on statistics of v_n, based on which they carried out the optimum Δt for their case. Following this idea, the mean and r.m.s. entrainment velocities at different streamwise positions are examined against the advection time interval Δt as shown in figure 8(*b*,*c*). It is found that when the time interval is large ($\Delta t > 0.6\tau_\eta$,

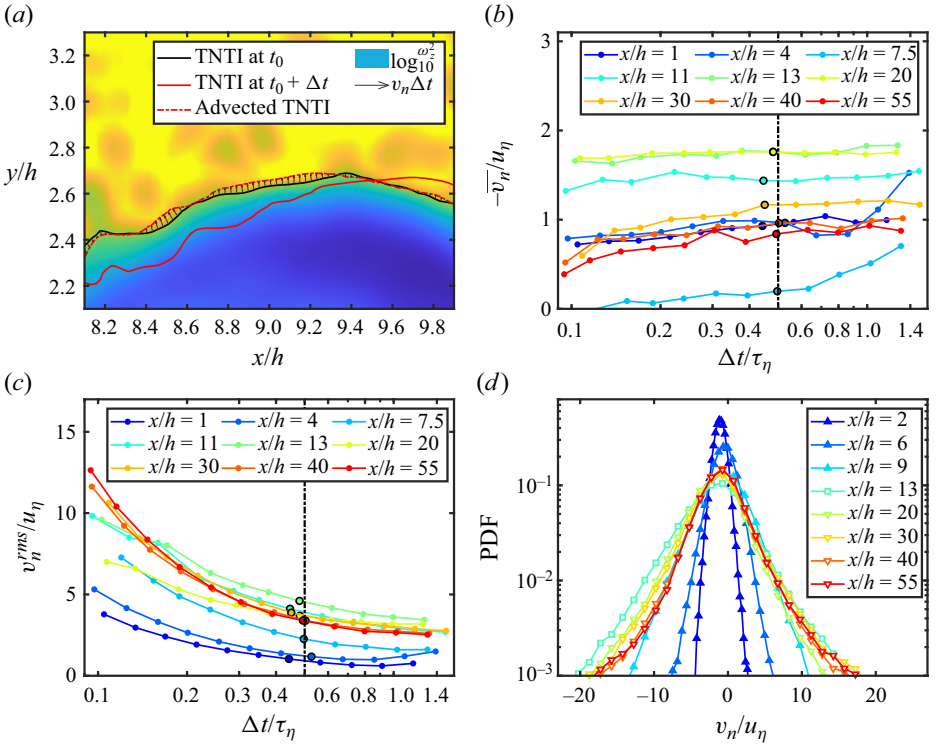

Figure 8. (*a*) Illustration of the entrainment velocity calculation process. (*b*) Variation of the time-mean entrainment velocity $\overline{v_n}$ against the advection time Δt. (*c*) Variation of the r.m.s. entrainment velocity v_n^{rms} against the advection time Δt. (*d*) The PDFs of entrainment velocity at different streamwise positions for $\Delta t = 4\tau_\eta$.

where $\tau_\eta = (\nu/\varepsilon_I)^{1/2}$ is the local Kolmogorov time scale at the TNTI), magnitudes of the mean entrainment velocity $\overline{v_n}$ increase with the increase of Δt at the positions where the flow evolves relatively quickly, for example, at $x = 4h$ and $7.5h$ as shown in figure 8(*b*). For other cases, $\overline{v_n}$ seems insensitive to Δt. On the other hand, as shown in figure 8(*c*), the r.m.s. entrainment velocity v_n^{rms} decreases with the increase of Δt because the larger spatial separation of TNTIs can improve the signal-to-noise ratio. Besides, even if different $\Delta t/\tau_\eta$ is used at the different streamwise positions, relative differences between entrainment velocities at different streamwise positions are qualitatively negligible. As a result, in the present work, Δt is selected as $0.5\tau_\eta$ at all streamwise positions as shown by the black dash-dotted line in figure 8(*b*,*c*), with the idea that the optimum Δt should make v_n^{rms} as small as possible while having little effect on $\overline{v_n}$ (Mistry *et al.* 2016). In fact, Δt can only be an integer multiple of the time resolution of data sets and τ_η varies along the streamwise direction, which means that Δt may not be exactly equal to $0.5\tau_\eta$ for all positions. Thus, the actual time interval closest to $0.5\tau_\eta$ is selected as shown by black hollow circles in figure 8(*b*,*c*), but is denoted as '$\Delta t = 0.5\tau_\eta$' for brevity.

The PDFs of v_n/u_η are shown in figure 8(*d*), where $u_\eta = (\nu\varepsilon_I)^{1/4}$ is the local Kolmogorov velocity scale at the TNTI. All PDFs are non-Gaussian and have negative skewness corresponding to the outwards spreading tendency of the turbulent region, which is qualitatively consistent with the previous results (Wolf *et al.* 2012; Mistry *et al.* 2016; Long *et al.* 2022*a*). For $x < 6h$ where vortex structures are relatively weak, the probability

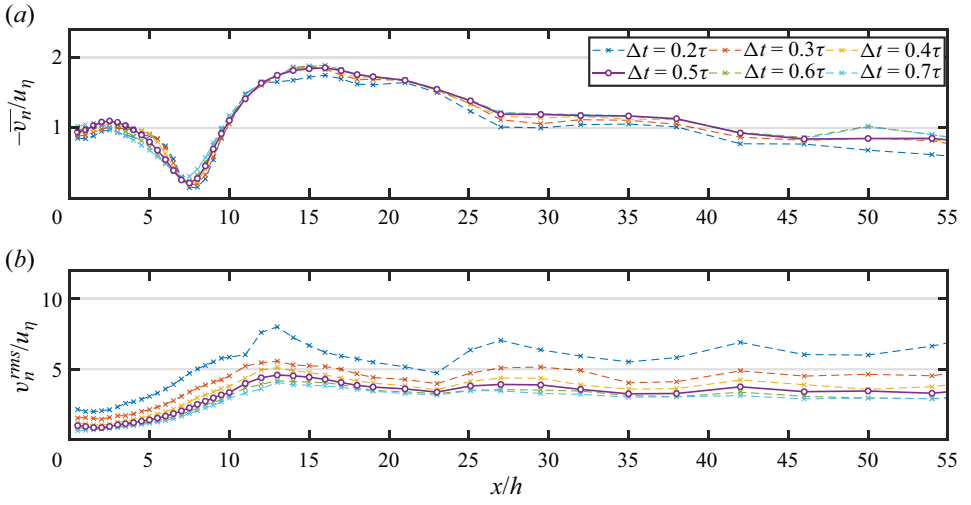

Figure 9. Streamwise variation of (*a*) the time-mean entrainment velocity $\overline{v_n}$ and (*b*) the r.m.s. entrainment velocity v_n^{rms}.

distribution of v_n is concentrated and changes slightly along the streamwise direction. After the deformation of the shedding vortex ($x > 6h$), the PDF of larger entrainment velocity increases significantly. Furthermore, the PDF of v_n/u_η grows slowly again after the breakdown of the shedding vortex ($x > 9.2h$). Finally, the PDF of larger v_n/u_η begins to decrease slightly after the reattachment ($x > 13h$) and becomes almost invariable far downstream when $x > 46h$. Obviously, the evolution of entrainment velocity is closely related to the vortex structure. More details about the effect of the vortex structure will be discussed in § 4.3.

To illustrate the evolution of the entrainment velocity more clearly, streamwise variations of the time-mean entrainment velocity $\overline{v_n}$ and the r.m.s. entrainment velocity v_n^{rms} are shown in figure 9. The results of selecting other Δt are also shown in this figure. Again, it shows that the error will be larger when $\Delta t \leq 0.3\tau_\eta$. Meanwhile, when $\Delta t \geq 0.7\tau_\eta$, the error due to the spatial evolution becomes more apparent in the vicinity of $x = 7.5h$. Therefore, it is appropriate to choose the compromise value of $\Delta t = 0.5\tau_\eta$ (all results hereinafter are based on $\Delta t = 0.5\tau_\eta$). For $x < 2h$, the separated flow is dominated by the shear motions and the change of $\overline{v_n}$ is quite small. When the prograde shedding vortex appears ($x > 2h$), the entrainment velocity begins to decrease. The magnitude of $\overline{v_n}$ decreases more rapidly when the vortex structure begins to deform due to secondary instability ($x > 6h$). The entrainment velocity is minimum at $x = 7.5h$ where the prograde vortex is the strongest. With the further deformation of the shedding vortex, the vortex structure is stretched more significantly in the vertical direction. The vorticity diffuses deeper into the boundary layer rather than concentrates near the TNTI, which reduces the effect of the prograde vortex structure on entrainment resulting in a gradual recovery in the entrainment velocity. After the breakdown of the shedding vortex, the entrainment velocity continues to increase and reaches the maximum magnitude of $\overline{v_n} = 1.85u_\eta$ after the reattachment. Then the entrainment velocity decreases and finally reaches a constant value of $0.85u_\eta$ for $x > 46h$, which is qualitatively consistent with results reported by previous studies for fully developed turbulence (Wolf *et al.* 2012; Mistry *et al.* 2016; Long *et al.* 2022*b*). On the other hand, the variation of v_n^{rms} is relatively simple and does not correspond to development stages of the shedding vortex. Here v_n^{rms} is quite small

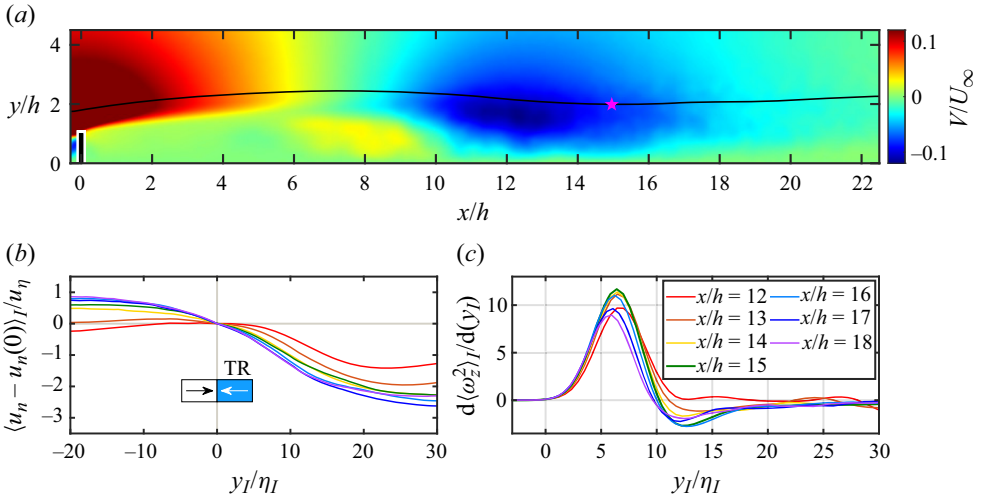

Figure 10. (*a*) Time-mean vertical velocity V and the time-mean height of the TNTI Y_i (denoted by the black curve). The minimal point of Y_i is marked by the magenta pentagram. (*b*) Conditional averaged relative normal velocity $\langle u_n - u_n(0)\rangle_I$. (*c*) Gradient of the conditional averaged enstrophy. Curves in (*b*) correspond to the same streamwise positions as those in (*c*).

when $x < 6h$ because the nibbling is mainly related to the viscosity in the early stage. It increases monotonically before the reattachment, and then slightly decreases to a plateau of $v_n^{rms} \approx 3.4u_\eta$.

Additionally, it is interesting to find that the maximum of $\overline{v_n}$ is associated well with the local minimal value of the mean TNTI height Y_i at $x \approx 15h$ in the reattachment region, where the sweep flow ($V < 0$) is strong as shown in figure 10(*a*). According to Long *et al.* (2022*a*), v_n will be enhanced when more fluids are transported towards the TNTI. Therefore, it is expectable that the flow in the vicinity of the TNTI in the reattachment region is not induced away from the TNTI by the sweep flow, and it is verified in figure 10(*b*) by checking the conditional averaged relative velocity $\langle u_n - u_n(0)\rangle_I$ in the vicinity of the TNTI. Here, u_n is the projected velocity on the TNTI normal direction and $u_n(0)$ is the u_n at the TNTI location. Because the TNTI normal vector points towards the turbulent region, $\langle u_n - u_n(0)\rangle_I > 0$ means the flow moves towards the turbulent region. Although the time-mean sweep flow is strong in the reattachment region, fluids in the turbulent region still move towards the TNTI ($\langle u_n - u_n(0)\rangle_I < 0$), which is conducive to nibbling (Long *et al.* 2022*a*). Moreover, the gradient of the conditional averaged enstrophy is largest at $x \approx 15h$ as shown in figure 10(*c*), which might also be responsible for the largest $\overline{v_n}$ there.

Nevertheless, a larger (smaller) entrainment velocity does not necessarily mean more (less) entrainment since the tortuous geometry of TNTI allows for a larger contact area between turbulent and non-turbulent regions (Mistry *et al.* 2016; Long *et al.* 2022*a*). Therefore, the contribution of nibbling is usually quantified by the nibbling flux F_n, which takes both the entrainment velocity and TNTI length into account. To study the variation of the flux along the streamwise direction, the local nibbling flux is calculated in a window with a finite width L_x and taken as the value at the centre position of that window. Besides, it is divided by L_x to contract the dependence on the window width, i.e.

$$F_n = \frac{1}{L_x}\int_{TNTI} v_n \,\mathrm{d}s, \tag{4.1}$$

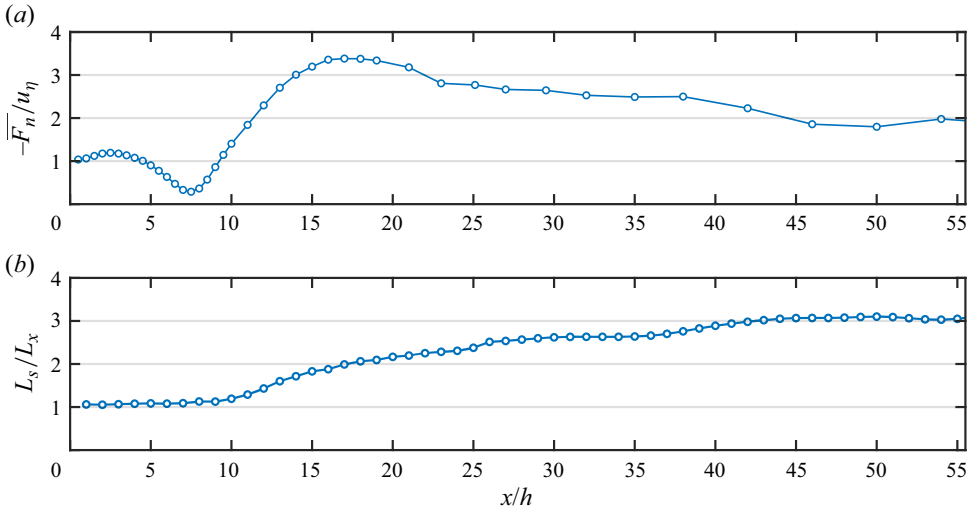

Figure 11. (*a*) Variation of the time-mean nibbling flux along the streamwise direction. (*b*) Tortuosities of the TNTI at different streamwise positions.

where ds is the length element. Here L_x is equal to 10 mm in the present work. A larger L_x will smooth the streamwise variation of results, but will not qualitatively affect the conclusions. Then, nibbling fluxes at different positions are obtained by shifting the window. Time-mean nibbling fluxes $\overline{F_n}$ and tortuosities of the TNTI at different streamwise positions are presented in figure 11(*a*,*b*), respectively, where the latter is approximately quantified by the ratio between the curve length of the TNTI, L_s, and L_x. The tortuosity of the TNTI grows monotonically along the streamwise direction from $L_s/L_x = 1$ (almost parallel to the wall) to $L_s/L_x = 3$ (fully distorted). However, when $\overline{v_n}$ is varying significantly, the TNTI has not been sufficiently distorted, resulting in the small effect of tortuosity on the nibbling flux. As a consequence, the variation trend of $\overline{F_n}$ is more similar to that of the mean entrainment velocity $\overline{v_n}$. This result implies that vortex structures affect the nibbling flux more by modulating the entrainment velocity than by increasing the tortuosity of the TNTI geometry in the transition process.

Since there are significant differences between vortex structures in the separated shear layer and that in the downstream newly developed turbulent boundary layer, it is natural to consider that the evolution of the entrainment velocity is closely related to the evolution of vortex structures. The effect of the vortex structure has been briefly mentioned when describing the evolution of entrainment velocity above, and it will be explained in more detail in § 4.3

4.2. *Entrainment characteristics: engulfment*

As for the engulfment process, because the engulfment process will generate low-vorticity bubbles in the turbulent region (Mathew & Basu 2002; da Silva *et al.* 2014*a*), we begin our studies on engulfment by investigating bubble structures. Bubbles are detected utilizing the same method and threshold as the TNTI detection. To avoid disturbance caused by noise, bubbles with an area smaller than 3×3 data points (approximately $3\eta_I \times 3\eta_I$) are ignored. Bubbles are widely distributed from the wall to the TNTI as shown in figure 12. However, not all of them are related to the engulfment process, because bubbles can also be generated inside the turbulent region instead of being engulfed from the

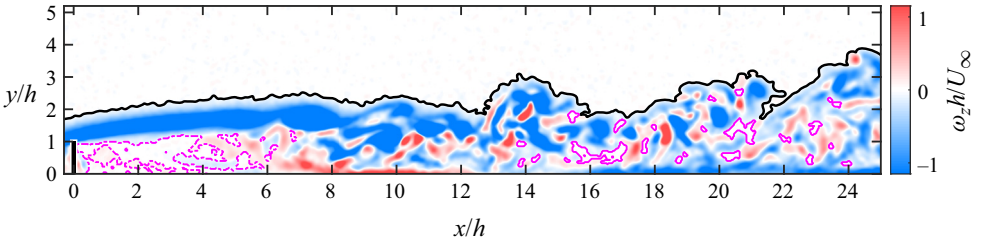

Figure 12. Instantaneous vorticity field downstream of the fence. The TNTI is denoted by the black curve, bubbles advected downstream are denoted by closed magenta solid curves, while bubbles advected upstream are denoted by closed magenta dash-dotted curves.

non-turbulent region (da Silva, Taveira & Borrell 2014*b*). Besides, low-vorticity regions in the recirculation zone will also be identified as bubbles as shown by dash-dotted curves in figure 12. Nevertheless, bubbles in the recirculation zone are unlikely to be associated with engulfment, as the recirculation zone is isolated from the free stream by the separated shear layer. Therefore, bubbles advected upstream are excluded.

Furthermore, it was found that the size of bubbles (Jahanbakhshi & Madnia 2016), the velocity fluctuations inside bubbles (Long *et al.* 2022*a*) and the homogeneity of the flow inside bubbles (Xu *et al.* 2023) show significant differences between bubbles near and away from the TNTI. These characteristics vary considerably with the distance from the bubble to the TNTI, but they are approximately constant when the bubble is located deep inside the turbulent core region. In addition, PDFs of bubble size near and far away from the TNTI follow different power laws. The latter follows the power law with an exponent of -3 that is consistent with that reported in the homogeneous isotropic turbulence (da Silva *et al.* 2014*b*), suggesting that bubbles far away from the TNTI are more likely to be generated inside the turbulent region. Therefore, an approach to separate engulfment-induced bubbles from the others based on the distance from the bubble to the TNTI has been implemented in previous studies (Jahanbakhshi & Madnia 2016; Long *et al.* 2022*a*; Xu *et al.* 2023). Moreover, Wu, Wang & Pan (2020) studied the trajectory of bubbles in the turbulent boundary layer and reported that the y-coordinate of the bubble centroid is almost constant during the advection, which indicates that bubbles generated by engulfment are usually not advected deeper into the turbulent core region. This evidence also supports the feasibility of the method that distinguishes the two kinds of bubbles based on their distances to the TNTI.

In the present study, the critical distance is determined by examining the homogeneity of the flow in bubbles, which is measured by the velocity standard deviation within the bubble (Xu *et al.* 2023),

$$\sigma_b = \sqrt{\overline{(u - \langle u \rangle_b)^2}}, \tag{4.2}$$

where $\langle u \rangle_b$ is the spatially averaged velocity inside each bubble. The variations of $\langle \sigma_b \rangle$ against the distance Δ_{b-I} from the bubble to the TNTI are shown in figure 13(*a*), where $\langle \sigma_b \rangle$ is the conditional average of σ_b based on Δ_{b-I}. Curves of $\langle \sigma_b \rangle$ at $x = 7$–$11h$ are greatly fluctuant probably because the number of bubbles at the beginning of appearance is not enough to ensure the convergence of statistical results. Along the streamwise direction, $\langle \sigma_b \rangle$ decreases gradually until the new turbulent boundary layer is fully developed for $x > 46h$, just as the disturbance caused by the flow separation gradually decays. When $x \geq 12h$, variations of $\langle \sigma_b \rangle$ against Δ_{b-I} become regular to some degree. Specifically, $\langle \sigma_b \rangle$ increases apparently when the bubble is near the TNTI, while it remains constant

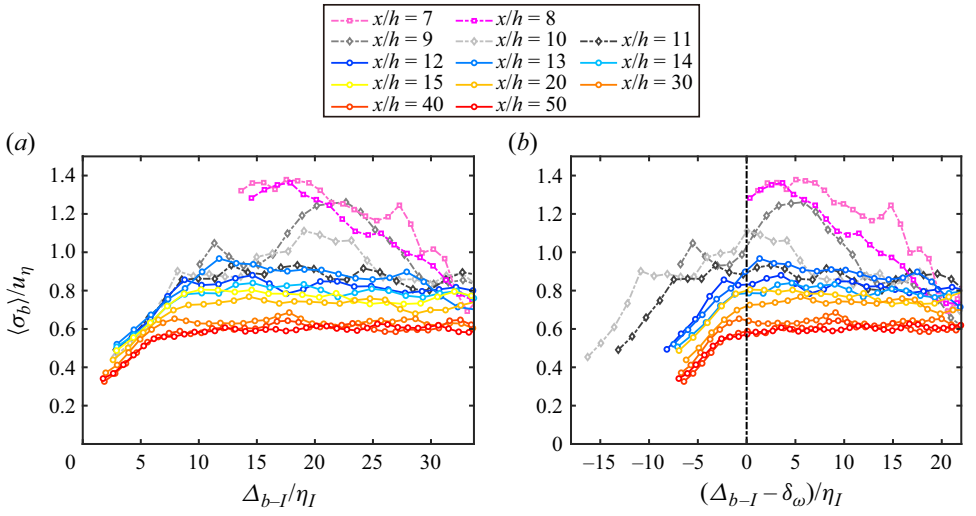

Figure 13. Conditional averaged velocity standard deviation inside bubbles $\langle\sigma_b\rangle$ as functions of (*a*) Δ_{b-I} and (*b*) $(\Delta_{b-I}-\delta_\omega)$, respectively, at different streamwise positions.

or slightly decreases when the bubble is far away from the TNTI. This result is in good agreement with that in jets reported by Xu *et al.* (2023).

Bubbles near the TNTI that contain more homogeneous flows are more likely to be generated by engulfment, such that it is natural to use the turning point of the $\langle\sigma_b\rangle - \Delta_{b-I}$ curve as the critical distance to distinguish the two kinds of bubbles. However, turning points at different streamwise positions are inconstant in the present study. Reviewing previous studies, the Taylor length scale (Jahanbakhshi & Madnia 2016) and 15η (Long *et al.* 2022*a*; Xu *et al.* 2023) (η is the Kolmogorov length scale) have been used as the threshold to distinguish the engulfed bubbles, which correspond exactly to the TNTI thickness in their cases, respectively. The TNTI thickness δ_ω in the present case is slightly different from that at high Reynolds number and varies along the streamwise direction (Li *et al.* 2022), prompting us to wonder whether the TNTI thickness is actually an adaptive threshold for all cases.

Therefore, curves of $\langle\sigma_b\rangle$ are offset by the local TNTI thickness δ_ω as shown in the figure 13(*b*). These results show that turning points at different streamwise positions coincide well with each other for $x \geq 12h$, as highlighted by the vertical dash-dotted line at $\Delta_{b-I} = \delta_\omega$. Although profiles are fluctuant in $x = 9$–$11h$, $\langle\sigma_b\rangle$ also increases and then decreases before and after $\Delta_{b-I} = \delta_\omega$ in general. Therefore, δ_ω is still used as a threshold in this region. Moreover, although bubbles appear as early as $x = 7$–$8h$, they are far away from the TNTI and contain more heterogeneous flow, and are more likely to be generated inside the turbulent region. On the other hand, PDFs of bubble size further corroborate this identification, as shown in figure 14. This result is in good agreement with that of previous studies (da Silva *et al.* 2014*b*; Jahanbakhshi & Madnia 2016; Long *et al.* 2022*a*; Xu *et al.* 2023). The PDFs of bubbles far away from the TNTI ($\Delta_{b-I} > \delta_\omega$) follow the power law with an exponent of -3, and PDFs of bubbles close to the TNTI ($\Delta_{b-I} < \delta_\omega$) follow a different power law with a larger slope of -4.4 in the present case. Therefore, only the bubbles inside the TNTI ($\Delta_{b-I} < \delta_\omega$) are taken into account for the estimation of engulfment in subsequent analyses.

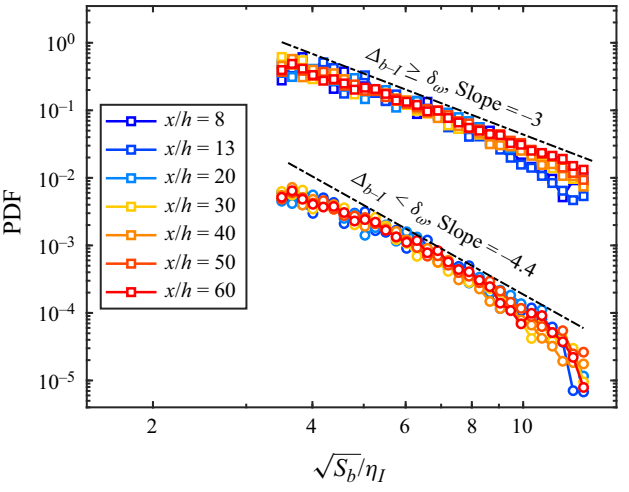

Figure 14. The PDFs of the bubble size at different streamwise positions. The bubble size is characterized by the square root of the bubble area S_b. The PDFs for $\Delta_{b-I} < \delta_\omega$ are offset by 10^{-2} for clarity.

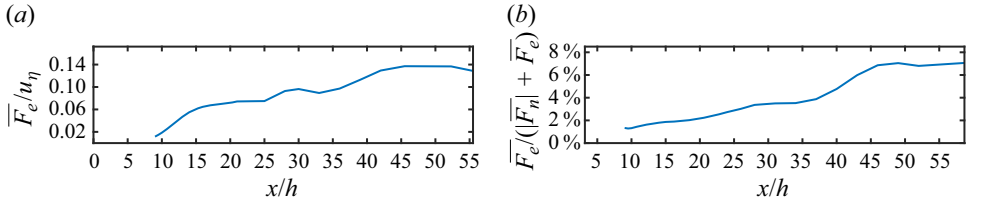

Figure 15. (*a*) Variation of the engulfment flux per wall unit $\overline{F_e}$ along the streamwise direction. (*b*) Proportion of the engulfment flux to the total entrainment flux.

Subsequently, the contribution of engulfment is quantitatively assessed by the time-mean engulfed area per unit length, $\overline{F_e}$, which is defined as the cumulative area of all engulfed bubbles over the entire experimental time span divided by the total time T and the length of the streamwise window L_x (identical to that in (4.1)), i.e.

$$\overline{F_e} = \frac{1}{T}\frac{1}{L_x}\sum_{\Delta_{b-I}<\delta_\omega} S_b. \tag{4.3}$$

In addition, it should be mentioned that, before summing the areas of bubbles, the advection trajectories of bubbles are tracked based on the time-resolved data and only the bubbles that emerged for the first time on each trajectory were counted to avoid repeatedly counting the same bubble from the Lagrangian perspective. The time-mean engulfed area $\overline{F_e}$ is shown in figure 15(*a*). The contribution of engulfment measured according to the method mentioned above becomes observable downstream after the breakdown of the shedding vortex. Here $\overline{F_e}$ increases rapidly in the region $x = 9.2$–$15h$, and then varies slightly after the reattachment zone. When the turbulent boundary layer is fully developed, $\overline{F_e}$ becomes approximately $0.14u_\eta$. Engulfment is generally related to large-scale motions in the flow (Westerweel *et al.* 2005; Jahanbakhshi & Madnia 2016), and can be enhanced by stronger sweep events (Long *et al.* 2022*a*). Therefore, the evident growth of $\overline{F_e}$ in $x = 9.2$–$15h$ might be related to the sweep flow near the reattachment point.

Furthermore, the contribution of engulfment to total entrainment is examined by comparing the time-mean area entrained by each of these two mechanisms, as already mentioned at the beginning of § 4. To avoid confusion, it should be noted that since nibbling is a continuous mechanism in time, the time-mean area entrained by nibbling is exactly equivalent to the time-mean nibbling flux $\overline{F_n}$. As a consequence, the method in the present work differs from that of Jahanbakhshi & Madnia (2016) and Long *et al.* (2022*a*) only in the quantification of engulfment. Figure 15(*b*) shows the proportion of the engulfed area $\overline{F_e}$ to the total entrained area ($|\overline{F_n}| + \overline{F_e}$). The proportion of $\overline{F_e}$ does not increases as rapidly as $\overline{F_e}$ in $x = 9.2h$–h, because the nibbling flux $\overline{F_n}$ in this region also increases significantly as shown in figure 11(*a*). Even thought this proportion steadily increases along the streamwise direction when $x < 46h$, it is only approximately 6.9 % when the turbulent boundary layer is fully developed, which is consistent with the result reported by Jahanbakhshi & Madnia (2016) (4–8 %) and Long *et al.* (2022*a*) (5.5 %) despite the difference in the quantification methods. In fact, assuming all bubbles close to the TNTI at a certain instant were engulfed into the turbulent region from the free stream, the contribution of engulfment to entrainment may have been over overestimated (Borrell and Jiménez 2016; Jahanbakhshi & Madnia 2016). However, under such estimation, the time-mean engulfed area is still much smaller than the nibbling flux, suggesting that the contribution of engulfment to total entrainment is indeed small.

4.3. *Effect of vortex structures on entrainment*

To better understand how the evolution of vortex structures leads to the variation of entrainment along the streamwise direction, the local effect of vortex structures on the entrainment is further studied. Since the nibbling process is dominant in entrainment, more attention has been paid to the influence of vortex structures on nibbling in the present study. Since entrainment is modulated by the vortex near the TNTI (Watanabe *et al.* 2017; Neamtu-Halic *et al.* 2020), only the prograde and retrograde vortices closest to the TNTI are extracted. Then the flow around these vortices are studied by means of the conditional analysis: data are recollected from frames centred at centroids of vortex structures at a certain streamwise position, and averaged based on relative coordinates to the frame origin. The streamwise and vertical coordinates in the conditional frame are normalized with the local radius of the vortex structure evaluated as $R = \sqrt{A_v/\pi}$, to compare the flow field around vortex structures of the same normalized size (Neamtu-Halic *et al.* 2020).

The conditional results are presented in figure 16. It is consistent with the previous understanding that the entrainment velocity v_n is modulated by the nearby vortex structure (Watanabe *et al.* 2017; Mistry *et al.* 2019; Neamtu-Halic *et al.* 2020). More specifically, v_n above and downstream of the prograde vortex structure is reduced while v_n upstream of the prograde vortex structure is enhanced. The entrainment velocity far away downstream of the prograde vortex structure at $\Delta x/R \approx 5$ is also enhanced in the early stage of transition as shown in figure 16(*a*,*b*). This might be related to the periodicity of vortex shedding, that is, the relative velocity towards the TNTI, which enhances the enstrophy production thus increasing the entrainment velocity (Long *et al.* 2022*a*), is induced by the downstream shedding vortex. This phenomenon fades away when the motion of vortex structures becomes more disordered. Besides, before the breakdown of the shedding vortex ($x < 9.2h$), the induced strong reduction of the entrainment velocity is located just above the prograde vortex structure, which is different with that after the breakdown of the shedding vortex ($x > 9.2h$). On the other hand, the retrograde vortex structure shows the opposite effect. Here v_n above and downstream of the retrograde vortex structure is enhanced, but there is no obvious decrease of v_n upstream of the retrograde vortex structure. Moreover,

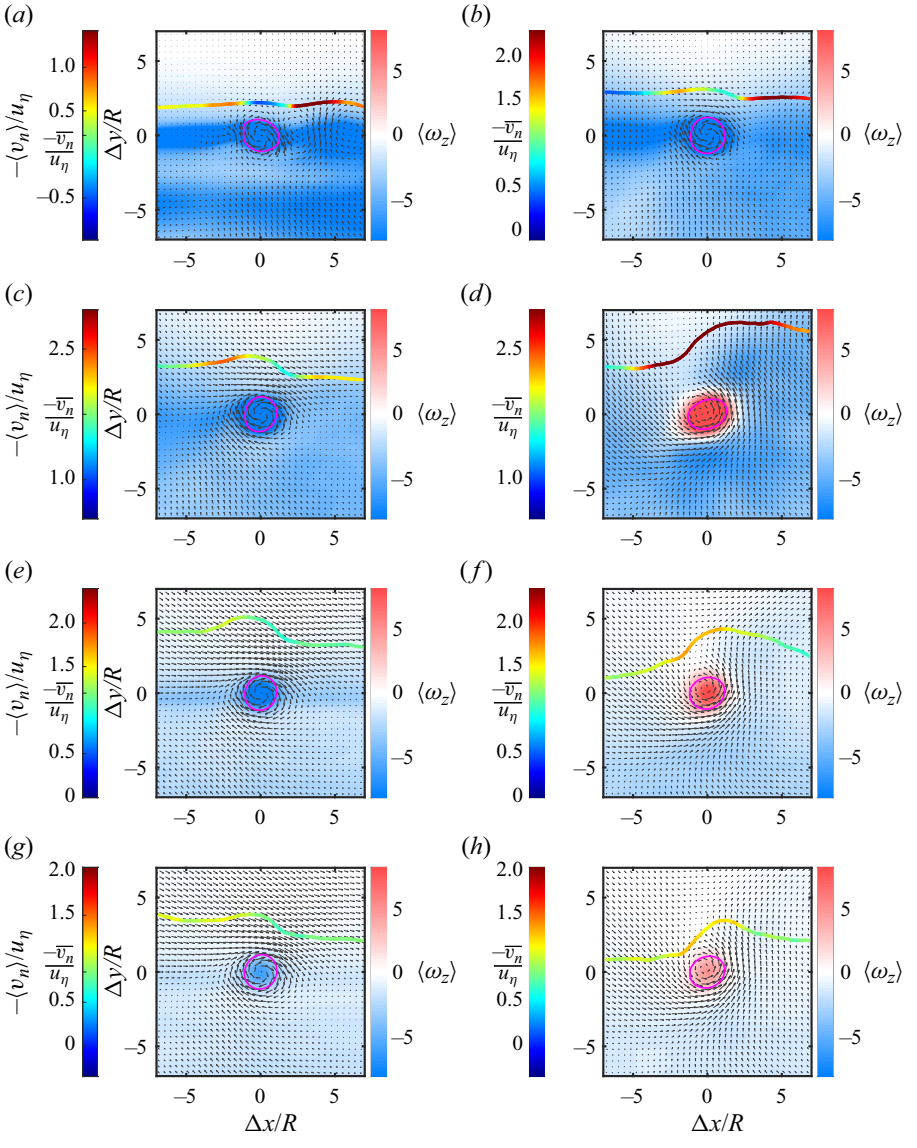

Figure 16. Conditional averaged flow fields in the vicinity of vortex structures. The conditional fluctuation velocity vectors are superimposed on the contour map of conditional averaged vorticity $\langle\omega_z\rangle$. The vortex structure boundary is indicated by the magenta contour of the conditional averaged swirling strength $\langle\lambda_{ci}\rangle = 0.2\langle\lambda_{ci}\rangle_{max}$. The conditional averaged position of the TNTI is presented by the jet-coloured open curve, whose colour represents the magnitude of conditioned averaged entrainment velocity $\langle v_n\rangle$. The colour bar of $\langle v_n\rangle$ (left) is centred at the ensemble averaged entrainment velocity $\overline{v_n}$ to make it convenient to identify the increase or decrease in the entrainment velocity through colour. Data for conditional analysis are obtained in the vicinity of (*a*,*b*,*c*,*e*,*g*) prograde and (*d*,*f*,*h*) retrograde vortex structures at (*a*) $x = 7.5h$, (*b*) $x = 10h$, (*c*,*d*) $x = 13h$, (*e*,*f*) $x = 30h$ and (*h*,*g*) $x = 55h$, respectively.

the conditional averaged position of the TNTI and entrainment velocity $\langle v_n\rangle$ are not as self-similar with respect to the size of vortex structures among different positions as they are in the fully developed turbulence reported by Neamtu-Halic *et al.* (2020). This is mainly the result of the flow itself not being self-similar in the transition process, so it

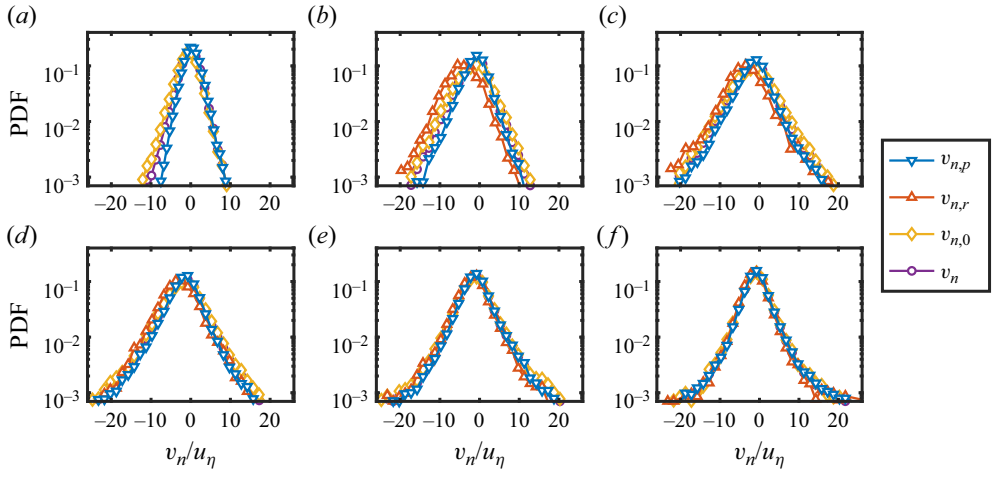

Figure 17. Conditional PDFs of entrainment velocity based on whether there is a prograde or retrograde vortex beneath the TNTI or no vortex beneath the TNTI. Entrainment velocities in the above three conditions are denoted by $v_{n,p}$, $v_{n,r}$ and $v_{n,0}$, respectively. Ensemble PDF of entrainment velocity v_n is also presented for comparison. Data sets are extracted at (*a*) $x = 7.5h$, (*b*) $x = 11h$, (*c*) $x = 13h$, (*d*) $x = 16h$, (*e*) $x = 30h$ and (*f*) $x = 46h$, respectively.

is difficult to normalize the effect of the vortex structure on entrainment based only on the structure size. Evidently, the effect of the vortex structure on entrainment is also related to the strength of the vortex and the distance from the vortex to the TNTI. After the turbulent boundary layer is fully developed, the conditional averaged field around both the prograde and the retrograde vortex structure becomes self-similar but the effect of the vortex is quite weak compared with that in the transition process.

To explore the difference in modulations of prograde and retrograde vortex structures on entrainment, conditional PDFs of entrainment velocity are investigated based on whether there is a prograde or retrograde vortex beneath the TNTI or no vortex beneath the TNTI, as shown in figure 17. Entrainment velocities extracted in the above three conditions are denoted by $v_{n,p}$, $v_{n,r}$ and $v_{n,0}$, respectively. Before the reattachment, the PDF of $v_{n,p}$ is smaller than PDFs of $v_{n,0}$ and v_n when $v_{n,p} < 0$, while it compares well with the PDFs of $v_{n,0}$ and v_n when $v_{n,p} > 0$. This result indicates that the prograde vortices will weaken the entrainment process ($v_n < 0$) but hardly affect the detrainment process ($v_n > 0$). However, the effect of retrograde vortices on the entrainment is not simply opposite to that of prograde vortices. The PDF of $v_{n,r}$ is larger than the PDFs of $v_{n,0}$ and v_n when $v_{n,r} < 0$, and meanwhile it is smaller than the PDFs of $v_{n,0}$ and v_n when $v_{n,r} > 0$. It suggests that retrograde vortices strengthen the entrainment process while suppressing the detrainment process. In addition, the effect of prograde vortices on smaller entrainment velocities is negligible after the reattachment, while the effect of retrograde vortices is persistent further downstream. When the boundary layer is fully developed ($x > 46h$), there is no significant difference between the PDFs in each condition, except for the influence of prograde and retrograde vortices on the larger entrainment velocity.

To study the streamwise variation of the effect on the nibbling process more clearly, the entrainment velocity and the nibbling flux are conditional averaged according to the existence of vortex structures beneath the TNTI, i.e.

$$\langle v_n \rangle_c = \frac{1}{T_c} \int_0^{T_c} v_{n,c} \, \mathrm{d}t, \tag{4.4}$$

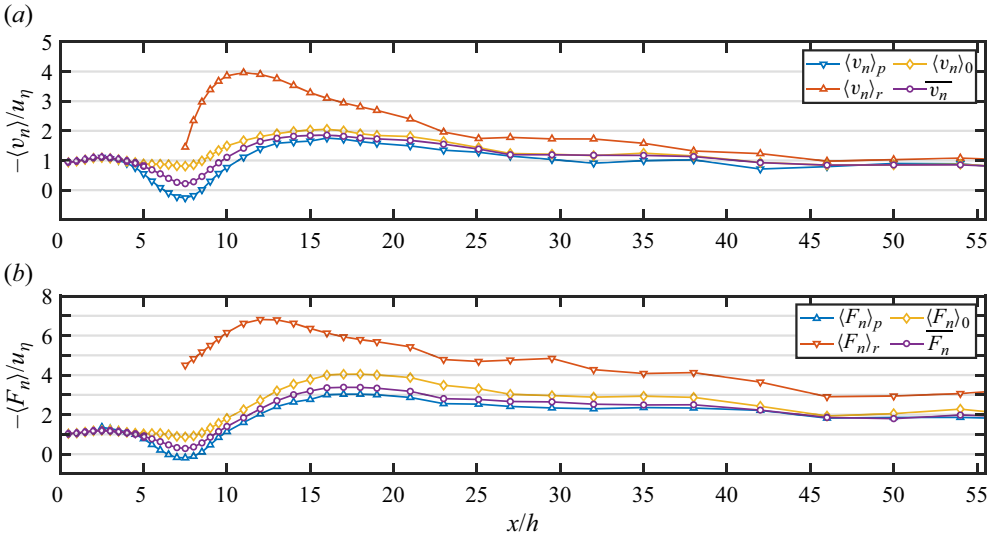

Figure 18. Streamwise variations of the conditional averaged (*a*) entrainment velocity $\langle v_n\rangle$ and (*b*) nibbling flux $\langle F_n\rangle$ based on whether there is a prograde, retrograde vortex or no vortex structure beneath the TNTI, respectively.

$$\langle F_n\rangle_c = \frac{1}{T_c}\int_0^{T_c}\frac{1}{L_x}\int_{TNTI} v_{n,c}\,\mathrm{d}s\,\mathrm{d}t, \tag{4.5}$$

where the subscript 'c' represents three different conditions, i.e. whether there is prograde, retrograde or no vortex structure beneath the TNTI, which is replaced by 'p', 'r', '0', respectively. Here $v_{n,c}$ and T_c are the entrainment velocity and the time period under the corresponding condition, respectively. When there is no vortex structure beneath the TNTI, the conditional averaged entrainment velocity $\langle v_n\rangle_0$ is almost constant when $x < 9.2h$ as shown in figure 18(*a*). Subsequently, $\langle v_n\rangle_0$ increases after the breakdown of the prograde shedding vortex, which might be related to the change in the enstrophy gradient when more small-scale vortices appear. Thereafter, the effect of vortex structure on entrainment is recognizable by comparing with the no-vortex case.

The retrograde vortex structure appears first in the region where the shedding vortex is deforming, which might be the two-dimensional slice of the streamwise leg of the horseshoe vortex evolved from the spanwise vortex (Hutchins, Hambleton & Marusic 2005). Around the retrograde vortex structures, the entrainment velocity is dramatically enhanced, with a maximum 2.4 times as large as that of $\langle v_n\rangle_0$ at $x = 11h$ where the retrograde vortex structure is the strongest. The strength of retrograde vortex structures becomes weakened when $x > 11h$, and $\langle v_n\rangle_r$ decreases monotonously until the boundary layer is fully developed ($x > 46h$). On the other hand, the prograde vortex shows an obvious suppression effect on the entrainment process, causing $\langle v_n\rangle_p$ to be smaller than $\langle v_n\rangle_0$ when $x > 4h$. The decrease of v_n does not occur from the generation of the prograde vortex in $x = 2$–$4h$, indicating that weak vortices generated in the early stage are difficult to affect entrainment. The prograde vortex structure is the strongest at $x = 7.5h$, which results in the greatest reduction of the entrainment velocity. It is noticeable that when the modulation of the prograde vortex is strongest in the vicinity of $x = 7.5h$, $-\langle v_n\rangle_p$ even becomes negative corresponding to the detrainment process. Note that, as shown in figure 17(*a*), this phenomenon is caused by the great suppression of prograde vortices

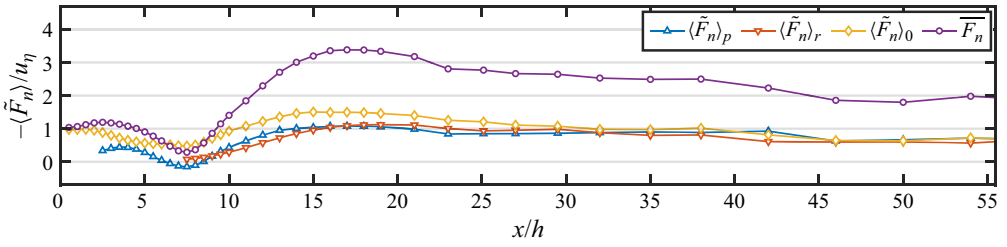

Figure 19. Streamwise variations of the conditional cumulated nibbling flux divided by the total time.

on entrainment instead of the enhancement on detrainment. After the breakdown of the shedding vortex, $-\langle v_n\rangle_p$ shows a similar variation trend with $\langle v_n\rangle_0$ as the effect of the prograde vortex weakens. When the boundary layer is fully developed, the conditional averaged entrainment velocities become constant, while the entrainment velocity above the retrograde vortex is still slightly larger than the other conditional averaged entrainment velocities. In addition, as already mentioned in § 4.1, due to the low tortuosity of the TNTI in the early stage, the overall variation trend of the conditional averaged nibbling flux is similar to that of the entrainment velocity as shown in figure 18(*b*). The conditional averaged entrainment flux above the retrograde vortex $\langle F_n\rangle_r$ is apparently larger than others even when the boundary layer is fully developed, which is related to the more distorted geometry of TNTI near the retrograde vortex.

It seems that the effect of retrograde vortex structures is dominant to the nibbling process because the conditional averaged nibbling flux above the retrograde vortex is much larger than the others. However, the variation trend of $\langle F_n\rangle_r$ does not coincide with that of the time-mean entrainment flux $\overline{F_n}$, which calls into question the importance of the modulation of retrograde vortices. In fact, if we consider the accumulated nibbling process over a long enough period of time, it becomes different because the frequency of retrograde vortices in the flow field is much less than that of prograde vortices, which means that retrograde vortex structures can not induce sustained enhancement on entrainment. To illustrate this problem more clearly, the conditional accumulated nibbling flux is investigated, defined as

$$\langle\tilde{F}_n\rangle_c = \frac{1}{T}\int_0^{T_c}\frac{1}{L_x}\int_{TNTI} v_{n,c}\,\mathrm{d}s\,\mathrm{d}t. \tag{4.6}$$

It is divided by the total time $T = T_p + T_r + T_0$ for comparison with the time-mean result since $\overline{F_n}T = (\langle\tilde{F}_n\rangle_p T_p + \langle\tilde{F}_n\rangle_r T_r + \langle\tilde{F}_n\rangle_0 T_0)$. As shown in figure 19, $\langle\tilde{F}_n\rangle_r$ is approximately as large as $\langle\tilde{F}_n\rangle_p$, while both of them are smaller than $\langle\tilde{F}_n\rangle_0$ before $x > 30h$. Therefore, it is not appropriate to attribute the rapid streamwise increase of time-mean nibbling flux around the reattachment point to the influence of retrograde vortices. As mentioned in § 4.1, the increase of the entrainment velocity is more likely to be related to the large enstrophy gradient near the TNTI and the relative movement of fluid towards the TNTI. Moreover, it is necessary to consider the frequency of vortex structures if entrainment is to be controlled or adjusted based on the effect of vortex structures.

5. Summary and conclusions

In this paper the evolution of entrainment in the transition process of the separated and reattaching flow induced by a wall-mounted fence and the effect of vortex structures on entrainment at low Reynolds number are studied by the time-resolved two-dimensional

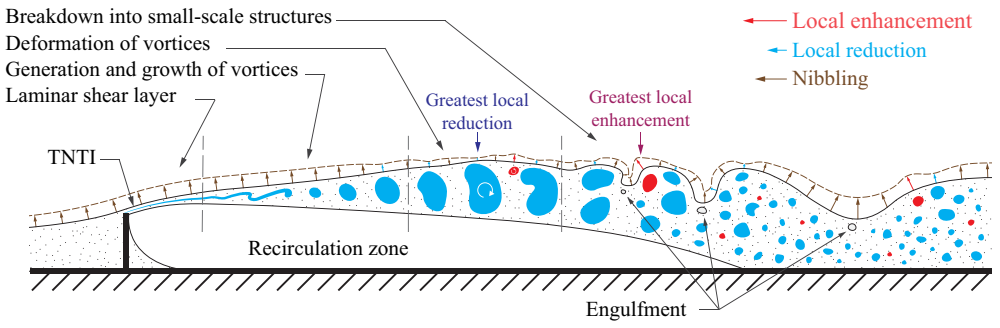

Figure 20. Summary of the entrainment evolution accompanied with the development of vortex structures.

PIV experiment. Significant variations of entrainment occur mainly above the recirculation zone and the reattachment zone. To understand the effect of the vortex on entrainment in more detail, the development of the separated shear layer is quantitatively divided into four stages according to the change of vorticity thickness growth rate, i.e. the stage of the laminar separated layer, the stage of vortex generation and development, the stage of vortex deformation and the stage after the shedding vortex breaks down. To the best of the authors' knowledge, this is the first investigation on entrainment of the separated and reattaching flow from the perspective of TNTI.

The evolution of entrainment and the effect of vortices are summarized in figure 20. Entrainment involves two mechanisms: nibbling and engulfment. In terms of the engulfment process, the earliest engulfment event occurs after the breakdown of the shedding vortex. However, the contribution of engulfment to entrainment is much less than that of nibbling in the whole process of flow evolution, which is consistent with the situation in jets and turbulent boundary layers. As for the nibbling process, it is shown that the prograde vortex near the TNTI reduces the entrainment velocity while the retrograde vortex shows the opposite behaviour. In more detail, the prograde vortex tends to suppress the entrainment process but has little effect on the detrainment process, while the retrograde vortex promotes the entrainment process and suppresses the detrainment process as well. In summary, among different flows such as jets and turbulent boundary layers, local nibbling is enhanced when more fluids in the turbulent region are transported towards the TNTI, while the opposite is true when more fluids move away from the TNTI, whether induced by vortex structures, large-scale motions or other coherent structures.

Certainly, the induced effect is related to the strength of the vortex structure, so the entrainment velocity can vary with the development of the vortex. The mean entrainment velocity is almost constant and the standard deviation of entrainment velocity is small in the stage of the laminar separated layer and the early stage of vortex development where there is no vortex beneath the TNTI or the vortex is weak. By the conditional average analysis, it is suggested that the strongest prograde vortex in the stage of vortex deformation leads to the greatest reduction in the mean entrainment velocity. Similarly, the greatest enhancement on the local entrainment velocity is induced by the strongest retrograde vortex in the stage after the breakdown of the shedding vortex. However, although the retrograde vortex can induce a significant enhancement on the local entrainment velocity, the long-term cumulative contribution of retrograde vortices to nibbling is not remarkable due to the scarcity of retrograde vortices near the TNTI. In fact, the largest mean entrainment velocity appears downstream of the reattachment point above the reattachment zone, where fluids in the vicinity of the TNTI are still transported

towards the TNTI and the conditional averaged enstrophy gradient is largest there. Besides, in the transition process the streamwise variation of the entrainment flux is similar to that of the entrainment velocity, indicating that variations of the entrainment velocity are more responsible for the development of the entrainment flux than the variation of the TNTI tortuosity, because the variation of the entrainment velocity is significantly larger than that of the tortuosity.

Funding. This work was supported by the National Natural Science Foundation of China (grant nos. 91852206 and 11721202).

Declaration of interests. The authors report no conflict of interest.

Author ORCIDs.
Sicheng Li https://orcid.org/0000-0002-8395-5480;
Jinjun Wang https://orcid.org/0000-0001-9523-7403.

References

Agelinchaab, M. & Tachie, M.F. 2008 PIV study of separated and reattached open channel flow over surface mounted blocks. *J. Fluid Engng* **130** (6), 061206.

Balamurugan, G., Rodda, A., Philip, J. & Mandal, A. 2020 Characteristics of the turbulent non-turbulent interface in a spatially evolving turbulent mixing layer. *J. Fluid Mech.* **894**, A4.

Bisset, D.K., Hunt, J.C.R. & Rogers, M.M. 2002 The turbulent/non-turbulent interface bounding a far wake. *J. Fluid Mech.* **451**, 383–410.

Borrell, G. & Jiménez, J. 2016 Properties of the turbulent/non-turbulent interface in boundary layers. *J. Fluid Mech.* **801**, 554–596.

Brown, G.L. & Roshko, A. 1974 On density effects and large structure in turbulent mixing layers. *J. Fluid Mech.* **64**, (4) 775–816.

Buxton, O.R.H. 2015 Modulation of the velocity gradient tensor by concurrent large-scale velocity fluctuations in a turbulent mixing layer. *J. Fluid Mech.* **777**, 1–12.

Castro, I. & Haque, A. 1987 The structure of a turbulent shear layer bounding a separation region. *J. Fluid Mech.* **179**, 439–468.

Champagnat, F., Plyer, A., Le Besnerais, G., Leclaire, B., Davoust, S. & Le Sant, Y. 2011 Fast and accurate PIV computation using highly parallel iterative correlation maximization. *Exp. Fluids* **50**, 1169–1182.

Chauhan, K., Philip, J. & Marusic, I. 2014 Scaling of the turbulent/non-turbulent interface in boundary layers. *J. Fluid Mech.* **751**, 298–328.

Cheng, Y. & Chen, Q. 2021 Large eddy simulation and dynamic mode decomposition of turbulent mixing layers. *Appl. Sci.* **11** (24), 12127.

Cimarelli, A. & Boga, G. 2021 Numerical experiments on turbulent entrainment and mixing of scalars. *J. Fluid Mech.* **927**, A34.

Corrsin, S. & Kistler, A.L. 1955 Free-stream boundaries of turbulent flows. *NACA Tech. Rep.* 3133.

Cui, G., Pan, C., Wu, D., Ye, Q. & Wang, J. 2019 Effect of drag reducing riblet surface on coherent structure in turbulent boundary layer. *Chin. J. Aeronaut.* **32** (11), 2433–2442.

Fang, X. & Tachie, M.F. 2019 On the unsteady characteristics of turbulent separations over a forward-backward-facing step. *J. Fluid Mech.* **863**, 994–1030.

Fang, X., Tachie, M.F. & Dow, K. 2022 Turbulent separations beneath semi-submerged bluff bodies with smooth and rough undersurfaces. *J. Fluid Mech.* **947**, A19.

Fiscaletti, D., Attili, A., Bisetti, F. & Elsinga, G.E. 2016*a* Scale interactions in a mixing layer the role of the large-scale gradients. *J. Fluid Mech.* **791**, 154–173.

Fiscaletti, D., Elsinga, G.E., Attili, A., Bisetti, F. & Buxton, O.R.H. 2016*b* Scale dependence of the alignment between strain rate and rotation in turbulent shear flow. *Phys. Rev. Fluids* **1**, 064405.

Fraga, V.S., Yin, G. & Ong, M.C. 2022 Three-dimensional numerical simulations and proper orthogonal decomposition analysis of flow over different bottom-mounted ribs. *Ships Offshore Struct.* **17** (4), 792–827.

George, W.K. & Hussein, H.J. 1991 Locally axisymmetric turbulence. *J. Fluid Mech.* **233**, 1–23.

Gu, H., Yang, J. & Liu, M. 2017 Study on the instability in separating-reattaching flow over a surface-mounted rib. *Intl J. Comput. Fluid Dyn.* **31** (2), 109–121.

HAYASHI, M., WATANABE, T. & NAGATA, K. 2021 The relation between shearing motions and the turbulent/non-turbulent interface in a turbulent planar jet. *Phys. Fluids* **33**, 055126.

HICKEY, J.-P., HUSSAIN, F. & WU, X. 2013 Role of coherent structures in multiple self-similar states of turbulent planar wakes. *J. Fluid Mech.* **731**, 312–363.

HOLZNER, M. & LUTHI, B. 2011 Laminar superlayer at the turbulence boundary. *Phys. Rev. Lett.* **106** (13), 134503.

HUTCHINS, N., HAMBLETON, W.T. & MARUSIC, I. 2005 Inclined cross-stream stereo particle image velocimetry measurements in turbulent boundary layers. *J. Fluid Mech.* **541**, 21–54.

JAHANBAKHSHI, R. 2021 Mechanisms of entrainment in a turbulent boundary layer. *Phys. Fluids* **33**, 035105.

JAHANBAKHSHI, R. & MADNIA, C. 2016 Entrainment in a compressible turbulent shear layer. *J. Fluid Mech.* **797**, 564–603.

KANG, N., ESSEL, E.E., ROUSSINOVA, V. & BALACHANDAR, R. 2021 Effects of approach flow conditions on the unsteady three-dimensional wake structure of a square-back Ahmed body. *Phys. Rev. Fluids* **6** (3), 034613.

KANKANWADI, K.S. & BUXTON, O.R.H. 2020 Turbulent entrainment into a cylinder wake from a turbulent background. *J. Fluid Mech.* **905**, A35.

VAN DER KINDERE, J. & GANAPATHISUBRAMANI, B. 2018 Effect of length of two-dimentional obstacles on characteristics of separation and reattachment. *J. Wind Engng Ind. Aerodyn.* **178**, 38–48.

LANDER, D.C., LETCHFORD, C.W., AMITAY, M. & KOPP, G.A. 2016 Influence of the bluff body shear layers on the wake of a square prism in a turbulent flow. *Phys. Rev. Fluids* **1**, 044406.

LI, S., LONG, Y. & WANG, J. 2022 Turbulent/non-turbulent interface for laminar boundary flow over a wall-mounted fence. *Phys. Fluids* **34**, 125113.

LIU, C., GAO, Y.-S., DONG, X.-R., WANG, Y.-Q., LIU, J.-M., ZHANG, Y.-N., CAI, X.-S. & GUI, N. 2019 Third generation of vortex identification methods: Omega and Liutex/Rortex based systems. *J. Hydrodyn.* **31**, 205–223.

LONG, Y., WANG, J. & PAN, C. 2022*a* Universal modulations of large-scale motions on entrainment of turbulent boundary layers. *J. Fluid Mech.* **941**, A68.

LONG, Y., WANG, J. & WANG, J. 2022*b* 'Turbulent/non-turbulent interface' in a low-Reynolds-number transitional boundary layer over a multi-element airfoil. *Phys. Fluids* **34**, 102111.

MARTHA, C.S., BLAISDELL, G.A. & LYRINTZIS, A.S. 2013 Large eddy simulations of 2-D and 3-D spatially developing mixing layers. *Aerosp. Sci. Technol.* **31** (1), 59–72.

MATHEW, J. & BASU, A.J. 2002 Some characteristics of entrainment at a cylindrical turbulence boundary. *Phys. Fluids* **14**, 2065–2072.

MISTRY, D., PHILIP, J. & DAWSON, J. 2019 Kinematics of local entrainment and detrainment in a turbulent jet. *J. Fluid Mech.* **871**, 896–924.

MISTRY, D., PHILIP, J., DAWSON, J.R. & MARUSIC, I. 2016 Entrainment at multi-scales across the turbulent/non-turbulent interface in an axisymmetric jet. *J. Fluid Mech.* **802**, 690–725.

MOHAMMED-TAIFOUR, A. & WEISS, J. 2016 Unsteadiness in a large turbulent separation bubble. *J. Fluid Mech.* **799**, 383–412.

MOORE, D.M., LETCHFORD, C.W. & AMITAY, M. 2019 Energetic scales in a bluff body shear layer. *J. Fluid Mech.* **875**, 543–575.

MORLET, J. 1983 Sampling theory and wave propagation. In *Issues in Acoustic Signal — Image Processing and Recognition* (ed. C.H. Chen), pp. 233–261. Springer.

NEAMTU-HALIC, M.M., KRUG, D., MOLLICONE, J., VAN REEUWIJK, M., HALLER, G. & HOLZNER, M. 2020 Connecting the time evolution of the turbulence interface to coherent structures. *J. Fluid Mech.* **898**, A3.

NEMATOLLAHI, A. & TACHIE, M.F. 2018 Time-resolved PIV measurement of influence of upstream roughness on separated and reattached turbulent flows over a forward-facing step. *AIP Adv.* **8**, 105110.

PAN, C., XUE, D., XU, Y., WANG, J. & WEI, R. 2015 Evaluating the accuracy performance of Lucas-Kanade algorithm in the circumstance of PIV application. *Sci. China-Phys. Mech. Astron.* **58**, 104704.

PHILIP, J., BERMEJO-MORENO, I., CHUNG, D. & MARUSIC, I. 2015 Characteristics of the entrainment velocity in a developing wake. In *International Symposium on Turbulence and Shear Flow Phenomena, TSFP-9, Melbourne, Australia*, vol. 3.

PHILIP, J. & MARUSIC, I. 2012 Large-scale eddies and their role in entrainment in turbulent jets and wakes. *Phys. Fluids* **24** (5), 055108.

PHILIP, J., MENEVEAU, C., DE SILVA, C.M. & MARUSIC, I. 2014 Multiscale analysis of fluxes at the turbulent/non-turbulent interface in high Reynolds number boundary layers. *Phys. Fluids* **26** (1), 015105.

QU, Y., WANG, J., FENG, L. & HE, X. 2019 Effect of excitation frequency on flow characteristics around a square cylinder with a synthetic jet positioned at front surface. *J. Fluid Mech.* **880**, 764–798.

RAJAGOPALAN, S. & ANTONIA, R.A. 2005 Flow around a circular cylinder – structure of the near wake shear layer. *Exp. Fluids* **38**, 393–402.

DA SILVA, C., HUNT, J.C.R., EAMES, I. & WESTERWEEL, J. 2014*a* Interfacial layers between regions of different turbulence intensity. *Annu. Rev. Fluid Mech.* **46** (1), 567–590.

DA SILVA, C.B., TAVEIRA, R.R. & BORRELL, G. 2014*b* Characteristics of the turbulent/nonturbulent interface in boundary layers, jets and shear-free turbulence. *Journal of Physics: Conference Series* **506** (1), 012015.

SILVA, T.S., ZECCHETTO, M. & DA SILVA, C.B. 2018 The scaling of the turbulent/non-turbulent interface at high Reynolds numbers. *J. Fluid Mech.J. Fluid Mech.* **843**, 156–179.

TAVEIRA, R.R., DIOGO, J.S., LOPES, D.C. & DA SILVA, C.B. 2013 Lagrangian statistics across the turbulent-nonturbulent interface in a turbulent plane jet. *Phys. Rev.* E **88**, 043001.

WATANABE, T., JAULINO, R., TAVEIRA, R.R., DA SILVA, C.B., NAGATA, K. & SAKAI, Y. 2017 Role of an isolated eddy near the turbulent/non-turbulent interface layer. *Phys. Rev. Fluids* **2**, 094607.

WATANABE, T., ZHANG, X. & NAGATA, K. 2018 Turbulent/non-turbulent interfaces detected in DNS of incompressible turbulent boundary layers. *Phys. Fluids* **30** (3), 035102.

WELCH, P. 1967 The use of fast Fourier transform for the estimation of power spectra: a method based on time averaging over short, modified periodograms. *IEEE Trans. Audio Electroacoust.* **15** (2), 70–73.

WESTERWEEL, J., FUKUSHIMA, C., PEDERSEN, J.M. & HUNT, J.C.R. 2005 Mechanics of the turbulent-nonturbulent interface of a jet. *Phys. Rev. Lett.* **95** (17), 174501.

WESTERWEEL, J., FUKUSHIMA, C., PEDERSEN, J.M. & HUNT, J.C.R. 2009 Momentum and scalar transport at the turbulent/non-turbulent interface of a jet. *J. Fluid Mech.* **631**, 199–230.

WHITE, F.M. 1991 *Viscous Fluid Flow*. Mcgraw-Hill.

WOLF, M., LÜTHI, B., HOLZNER, M., KRUG, D., KINZELBACH, W. & TSINOBER, A. 2012 Investigations on the local entrainment velocity in a turbulent jet. *Phys. Fluids* **24** (10), 105110.

WOLF, M., LÜTHI, B., HOLZNER, M., KRUG, D., KINZELBACH, W. & TSINOBER, A. 2013 Erratum: 'Investigations on the local entrainment velocity in a turbulent jet' [Phys. Fluids 24, 105110 (2012)]. *Phys. Fluids* **25**, 019901.

WU, D., WANG, J. & PAN, C. 2020 Bubbles and drops in the vicinity of turbulent/non-turbulent interface in turbulent boundary layer. *Exp. Fluids* **61**, 240.

WU, X., WALLACE, J.M. & HICKEY, J.P. 2019 Boundary layer turbulence and freestream turbulence interface, turbulent spot and freestream turbulence interface, laminar boundary layer and freestream turbulence interface. *Phys. Fluids* **31**, 045104.

WU, Y. & CHRISTENSEN, K.T. 2006 Population trends of spanwise vortices in wall turbulence. *J. Fluid Mech.* **568**, 55–76.

XU, C., LONG, Y. & WANG, J. 2023 Entrainment mechanism of turbulent synthetic jet flow. *J. Fluid Mech.* **958**, A31.

ZECCHETTO, M. & DA SILVA, C.B. 2021 Universality of small-scale motions within the turbulent/non-turbulent interface layer. *J. Fluid Mech.* **916**, A9.

ZHANG, H., RIVAL, D.E. & WU, X. 2021 Kinematics of the turbulent and nonturbulent interfaces in a subsonic airfoil flow. *AIAA J.* **59** (6), 2155–2168.

ZHANG, X., WATANABE, T. & NAGATA, K. 2018 Turbulent/nonturbulent interfaces in high-resolution direct numerical simulation of temporally evolving compressible turbulent boundary layers. *Phys. Rev. Fluids* **3**, 094605.

ZHANG, X., WATANABE, T. & NAGATA, K. 2023 Reynolds number dependence of the turbulent/non-turbulent interface in temporally developing turbulent boundary layers. *J. Fluid Mech.* **964**, A8.

ZHOU, J., ADRIAN, R.J., BALACHANDAR, S. & KENDALL, T.M. 1999 Mechanisms for generating coherent packets of hairpin vortices in channel flow. *J. Fluid Mech.* **387**, 353–396.